Geophysical Journal International

Geophys. J. Int. (2020) **222,** 169–188
Advance Access publication 2020 April 01
GJI Seismology

doi: 10.1093/gji/ggaa154

Understanding seismic path biases and magmatic activity at Mount St Helens volcano before its 2004 eruption

S. Gabrielli [1], L. De Siena [1,2] F. Napolitano [3] and E. Del Pezzo [4,5]

[1] *University of Aberdeen, School of Geosciences, AB24 3UE, Aberdeen, Scotland, UK. E-mail: ldesiena@uni-mainz.de, lucadesiena@abdn.ac.uk*
[2] *Institute of Geosciences, Johannes Gutenberg University, D-55128, Mainz, Germany*
[3] *Dipartimento di Fisica "E.R.Caianiello", Universitá degli Studi di Salerno, 84084, Fisciano (SA), Italy*
[4] *Istituto Nazionale di Geofisica e Vulcanologia, Sezione di Napoli-Osservatorio Vesuviano, 80124, Napoli, Italy*
[5] *Instituto Andaluz de Geofisica, Universidad de Granada, 18071, Granada, Spain*

Accepted 2020 March 25. Received 2020 March 25; in original form 2019 June 12

SUMMARY

In volcanoes, topography, shallow heterogeneity and even shallow morphology can substantially modify seismic coda signals. Coda waves are an essential tool to monitor eruption dynamics and model volcanic structures jointly and independently from velocity anomalies: it is thus fundamental to test their spatial sensitivity to seismic path effects. Here, we apply the Multiple Lapse Time Window Analysis (MLTWA) to measure the relative importance of scattering attenuation vs absorption at Mount St Helens volcano before its 2004 eruption. The results show the characteristic dominance of scattering attenuation in volcanoes at lower frequencies (3–6 Hz), while absorption is the primary attenuation mechanism at 12 and 18 Hz. Scattering attenuation is similar but seismic absorption is one order of magnitude lower than at open-conduit volcanoes, like Etna and Kilauea, a typical behaviour of a (relatively) cool magmatic plumbing system. Still, the seismic albedo (measuring the ratio between seismic energy emitted and received from the area) is anomalously high (0.95) at 3 Hz. A radiative-transfer forward model of far- and near-field envelopes confirms this is due to strong near-receiver scattering enhancing anomalous phases in the intermediate and late coda across the 1980 debris avalanche and central crater. Only above this frequency and in the far-field diffusion onsets at late lapse times. The scattering and absorption parameters derived from MLTWA are used as inputs to construct 2-D frequency-dependent bulk sensitivity kernels for the *S*-wave coda in the multiple-scattering (using the Energy Transport Equations—ETE) and diffusive (AD, independent of MLTWA results) regimes. At 12 Hz, high coda-attenuation anomalies characterize the eastern side of the volcano using both kernels, in spatial correlation with low-velocity anomalies from literature. At 3 Hz, the anomalous albedo, the forward modelling, and the results of the tomographic imaging confirm that shallow heterogeneity beneath the extended 1980 debris-avalanche and crater enhance anomalous intermediate and late coda phases, mapping shallow geological contrasts. We remark the effect this may have on coda-dependent source inversion and tomography, currently used across the world to image and monitor volcanoes. At Mount St Helens, higher frequencies and deep borehole data are necessary to reconstruct deep volcanic structures with coda waves.

Key words: North America; Coda waves; Seismic attenuation; Seismic tomography; Volcano seismology; Wave scattering and diffraction.

1 INTRODUCTION

Mount St Helens (MSH) is a stratovolcano of the Cascadian volcanic arc, one of the most active in the United States. On 18 May 1980, a magnitude-five earthquake triggered the collapse of a large sector of the northern part of the volcano, depressurising the hot rocks in the volcano's core. The earthquake unleashed a violent explosive outburst and a subsequent Plinian eruption that produced the largest landslide-debris avalanche recorded in historic time (Scandone & Malone 1985). After 18 yr of relative quiescence, MSH erupted again in 2004, when a lava spine grew upward the crater area, followed by several smaller spines and a whaleback-shaped extrusion (Vallance *et al.* 2008). An increased level of seismicity and the occurrence of seismic swarms are generally a reliable forecasting

signal for a volcanic eruption; however, the tectonic seismicity in the 4 yr before the 2004 eruption was low (both in magnitude and number) and sparse (Moran *et al.* 2008). Small-magnitude, shallow earthquakes occurred only a few days before the growth of a lava dome, followed by an uplift of the Crater Glacier, grown in the crater after the 1980 eruption (Schilling *et al.* 2004). The deep, sparse seismicity recorded between 2000 and 2003 seems unrelated to the 2004 eruption, as the volcano was in a near-eruptive equilibrium state long before (Iverson *et al.* 2006). Coda-wave attenuation (Q^{-1}) can map the structures and dynamics underlying such heterogeneous seismic patterns.

Coda waves are random wave trains, arriving much later than the *S*-wave direct arrivals and holding valuable information about the loss of seismic energy inside the medium. This loss is a proxy of the presence of melt and fluids in the crust, tectonic stress, and eruptive behaviour of a volcano (De Siena *et al.* 2016): still, the physical mechanism behind this loss (Q^{-1}) is uncertain. The main factors controlling Q^{-1} are scattering loss due to the heterogeneity in the crust (Q_s^{-1}) and absorption due to anelasticity (Q_i^{-1}) (Sato *et al.* 2012). The Multi Lapse Time Window Analysis (MLTWA, Fehler *et al.* 1992) is the most common method to discriminate between these two attenuation mechanisms from seismic data. The technique retrieves the Seismic Albedo B_0 (ratio between scattering and total coda attenuation, ranging between 0 and 1) and the Extinction Length (L_e, reciprocal of the total attenuation). These quantities can be related to eruptive and tectonic activity as well as to the presence of fluids and gasses at lithospheric scale (Mayeda *et al.* 1992; Canas *et al.* 1998; Dutta *et al.* 2004; Badi *et al.* 2009; Del Pezzo *et al.* 2015).

The MLTWA is a standard technique in regional settings, where it shows a predominance of either scattering or absorption depending on tectonic activity and frequency. As an example, in south-central Alaska (Dutta *et al.* 2004) Q_i^{-1} prevails on Q_s^{-1} at higher frequencies ($\geq$3.0 Hz) with a $B_0 < 0.48$ in the frequency range 1.0–6.0 Hz, marking the stability and low heterogeneity of the area. The MLTWA results of NE India (Padhy & Subhadra 2013) have a value of B_0 higher than 0.5 at low frequencies ($f <$ 3Hz) and lower than 0.5 at high frequencies ($f >$ 3Hz). This high albedo values suggest a frequency dependence due to the scale length of the lithospheric heterogeneity (about 1 km). In a few volcanic settings, the MLTWA results show a similar prevalence of intrinsic absorption over scattering below 10 Hz. The typical example is the Canary Island area (Canas *et al.* 1998) for hypocentral distances ranging between 0–80 km and 0–140 km. Nevertheless, in most local volcanoes, the MLTWA results show higher scattering than intrinsic attenuation over the entire frequency spectrum (Del Pezzo *et al.* 2015). Typical examples of this behaviour are Mt Asama (Prudencio *et al.* 2017) and the Galeras Volcanic Complex (Ugalde *et al.* 2010). Of particular interest for comparison with MSH are volcanoes with glaciers or snow-cover sitting in their caldera/cone, like Klyuchevskoi, in Kamchatka (Lemzikov 2008), Deception Island (Prudencio *et al.* 2013b) and Etna (Del Pezzo *et al.* 2019). Mayeda *et al.* (1992) show that this is also true in three different active volcanic regions at frequencies lower than 6 Hz: Hawaii, Long Valley and Central California. In the three regions, absorption dominates at higher frequencies. Open-conduit, active and dormant volcanoes mostly show a similar decreasing scattering behaviour with increasing frequency. However, intrinsic attenuation, observed at dormant or inactive volcanoes, like Mt Vesuvius (Bianco *et al.* 1999) and Mt Fuji (Chung *et al.* 2009), is one order of magnitude lower than in active ones, like Mt Etna (Del Pezzo *et al.* 2019). Chung *et al.* (2009) interpret this difference as due to the lack of the magmatic activity in the upper volcanic structures of Mt Fuji.

The results of the MLTWA analysis can be used as input for building 2-D and 3-D kernels in Q^{-1} imaging at regional scale (e.g. Obermann *et al.* 2013; Margerin *et al.* 2015). Kernel-based coda-attenuation techniques have been particularly successful in volcanic areas improving imaging and interpretation at all scales (Prudencio *et al.* 2013a, b, 2015). Typically, the sensitivity maxima are at source and station locations, and sensitivity decreases at a distance controlled by the extinction length (extinction distance over which the primary S wave is decreased by e^{-1}). Del Pezzo *et al.* (2016) designed diffusive kernels targeting volcanic settings: these kernels are most appropriate for imaging volcanic edifices and shallow caldera structures, where even early seismic signals are diffusive (Wegler & Lühr 2001; De Siena *et al.* 2013). They provide better spatial estimates of sensitivity in highly heterogeneous media, as they increase the illumination of the attenuation models recovered in volcanoes and are related to the diffusive process. Recent examples are Campi Flegrei caldera, where they provide the first seismic image of the primary deformation source (De Siena *et al.* 2017), and Long Valley caldera (Prudencio *et al.* 2018).

Still, a diffusive kernel is only applicable if diffusion rules the coda wavefields at the chosen lapse times. While volcanoes are often assumed as half-space or layered media, De Siena *et al.* (2013) shows the difficulty of forward-modelling envelopes using a unique scattering regime at Campi Flegrei caldera without including vertical or oblique boundaries. The existence of strong near-receiver scattering in heterogeneous media can enhance anomalous phases and block the onset of diffusion at late lapse times. This is especially true if this scattering couples body and surface waves (Larose *et al.* 2005a), breaking the hypothesis of bulk propagation underlying both MLTWA and sensitivity kernels (Obermann *et al.* 2013). Sanborn *et al.* (2017) have developed a computer code RADIATIVE3D for seismic radiative transport modelling that can be used to test the hypothesis of bulk-wave composition in the coda. The parameters describing scattering heterogeneity (velocity fluctuations ϵ and correlation length a) and absorption suffer consistent trade offs when modelling crustal reverberations at the regional scale Cormier & Sanborn (2019). The authors show that 3 Hz is the transition frequency between the lower scattering ($\epsilon^2 a = constant$) and higher scattering ($\frac{\epsilon^2}{a} = constant$) regimes in the crust. Using RADIATIVE3D to forward model envelopes, researchers can account for both horizontal and vertical interfaces, but disregard surface waves. At MSH and without active magma dynamics this application can inform if a bulk sensitivity kernel in a half-space is sufficient to forward-model recorded envelopes despite the presence of shallow unconsolidated materials.

To image Q^{-1} variations in the MSH area and separate scattering from absorption contributions, De Siena *et al.* (2016) have used coda-attenuation imaging together with peak-delay mapping. Their mapping of Q^{-1} is based on simplistic 'ray' assumptions, which do not model the sensitivity of coda-waves to the multiple-scattering medium. Here, we provide a new kernel-based 2-D coda attenuation image of the MSH cone and surroundings; to do so, we use the open-access MuRAT package (De Siena *et al.* 2014), currently available in its 2.0 version—see acknowledgment section. The code uses analytic diffusive kernel functions (Del Pezzo *et al.* 2016) to invert for Q^{-1} in space, with the inversion matrix being independent of frequency. While these kernels have been shown to provide inexact results when applied to model envelopes from deep volcanic seismicity (Del Pezzo *et al.* 2018), they are still an improvement of

the previous line-regionalization approach (De Siena *et al.* 2016). Then, the MLTWA results are used as input to reconstruct exact frequency-dependent kernels based on the Paasschens' approximation of the Energy Transport Equation solution in three dimensions, and for a multiple scattering regime (Paasschens 1997; Del Pezzo *et al.* 2018). Q^{-1} is mapped after downscaling the 3-D frequency-dependent kernels to 2-D, in order to compare the results of the two kernel-based inversions and discuss their improvements in terms of (1) data fit, (2) resolution and (3) stability versus ray-dependent attenuation maps of the area (De Siena *et al.* 2014, 2016). The hypotheses underlying both MLTWA and sensitivity kernels are tested with radiative transfer simulations in a half-space using RADIATIVE3D (Sanborn *et al.* 2017). Coda waves are currently used in source inversion modelling as a proxy of hydrothermal and magmatic dynamics for this and other volcanoes (e.g. Matoza & Chouet 2010; Matoza *et al.* 2015); we will thus discuss the impact of our results in the broader framework of source- and path-dependent imaging of volcanoes.

2 GEOLOGICAL AND GEOPHYSICAL SETTINGS

MSH is located in an atypical position, being 54 km trenchward of Mount Adams, misaligned with the rest of the volcanic arc. Regional seismic patterns and geologic features mark a NNW–SSE trending 'St Helens' Seismic Zone (SHZ) (Musumeci *et al.* 2002). This zone extends along a distance of 90 km, beneath and to the north of MSH, producing seismic events of predominantly dextral slip (Weaver & Smith 1983). The SHZ is a fault zone with the capacity of generating moderate-to-big shallow earthquake (Weaver & Smith 1983; Stanley *et al.* 1996). This alignment coincides with the contact between the Cascade arc crust and the mafic Coast Range basement (Siletz terrane), imaged as the main feeding path for the volcano (Parsons *et al.* 2006). Still, MSH presents eruptive products of various composition, from basalt to dacite, indicating one or more upper-crustal magma chambers. In particular, magnetotelluric results (Hill *et al.* 2009a) suggested that the feeding system of the volcano is a 15 km depth conduit, which dips east at around 15 km depth to an area of partial melt in the mid-crust. Anyway, the complexity of this feeding system is still not well known.

Seismic velocity tomography is an obvious choice to discriminate between the different interpretations of MSH feeding system. Natural earthquakes today are sparse at MSH, effectively biasing earthquake tomography inversions. Still, in the past the widely spread seismicity associated to the 1980 and 2004 eruptions and the installation of new seismic arrays allowed to image the volcano using body-wave information (e.g. Waite & Moran 2009). Earthquake tomography performed by Lees (1992, 2007) found a vertical high-velocity anomaly, inferred as an extinct magma body, penetrated by new dykes during the eruption of 1980 (Pallister *et al.* 1992). Later on, Waite & Moran (2009) showed an open system, with a 5 km deep-magmatic chamber feeding the 2004 eruption. More recently, the active-source seismic data of the iMUSH experiment shed new light on feeding structures (Kiser *et al.* 2016, 2018). At lithospheric scale, the derived seismic velocity studies interpret velocity anomalies in terms of lateral migration of the melt from the hotter region of the arc into the cooler forearc (Hansen *et al.* 2016), suggesting a source region in the eastern area towards Mt Adams similar to that proposed by Hill *et al.* (2009b). The iMUSH experiment also revealed a high *Vp*/*Vs* anomaly sitting beneath the volcano, between 4 and 13 km depth (Kiser *et al.* 2016), interpreted as the primary upper-middle crustal magma reservoir. Beneath this reservoir, also extending towards SE, a low *Vp* anomaly column extends from 15 km depth to the Moho, with long-period events located near its boundary (Hansen *et al.* 2016): these events indicate that the anomaly is associated with injection of magmatic fluids. In the same study, two velocity anomalies show that there are at least two feeding systems of MSH.

Even if the improvements in seismic imaging following iMUSH are relevant, active seismic imaging using coherent high-frequency waves loses resolution and reliability at depth. This bias is due to the presence of high-impedance vertical and lateral contrasts, which may trap energy near the surface (De Siena *et al.* 2016) and hide fluid reservoirs at depth (Eide *et al.* 2018). Coda wave attenuation is a marker of these effects; understanding their sensitivity can ideally provide relevant information about the eruptive activity of MSH. Fehler *et al.* (1988) first measured coda attenuation (Q^{-1}) for earthquakes recorded before, during and after the eruption of 3–6 September 1981. Q^{-1} was 20–30 per cent higher before the eruption than after, for frequencies between 6 and 30 Hz. Authors interpreted this behaviour as an increase of the opened microcracks, associated with the inflation of the volcano before the eruption. A peak of Q^{-1} near 10 Hz was attributed to scattering attenuation and to the scale length of heterogeneity that generates backscattered waves. This behaviour was confirmed two months before a volcanic crisis of Nevado del Ruiz volcano (Londono 1996), just after a period of stability of 2 yr. A similar decrease in attenuation, but for direct waves, was observed before and after seismic swarms, this time likely induced by the inflation of the magmatic chamber 10 yr after the dome-building eruption in 1986 (Tusa *et al.* 2004).

Q^{-1} mapping, *P*-wave attenuation tomography and *S*-wave scattering tomography were used to image the MSH volcanic system in both 3-D and 2-D (De Siena *et al.* 2014, 2016). The volcanic edifice and magma/fluid feeding zones appear as high-frequency high-attenuation and high-scattering anomalies. Besides, an almost linear high-scattering and high-attenuation zone in the northern sector of the volcano was attributed to the Tertiary marine sediments of the St Helens Seismic Zone (SHZ). At low frequencies (3 and 6 Hz), the authors show how high scattering and absorption anomalies were induced by the presence of the MSH 1980 debris avalanche north and northwest of the volcano, allowing to map the avalanche contours (De Siena *et al.* 2016). This work suggests that shallow heterogeneous layers may bias imaging in deep multiple-scattering volcanic settings.

3 DATA AND METHODS

The data set comprises 64 earthquakes occurred between 2000 and November 2003, characterized by magnitudes ranging from 1.5 to 2.6 and recorded by the Pacific Northwest Seismic Network, composed of 14 one-component stations installed in the area (Fig. 1). Even if we have just one component, Fehler *et al.* (1992) showed how, for the MLTWA and at MSH, the results using vertical components and horizontal ones are similar, as coda waves are mainly composed of shear energy in the diffusive regime. De Siena *et al.* (2017) validate the use of vertical components to study *S* waves in the diffusive regime at Campi Flegrei volcano. The authors obtain lapse-time-dependent maps of coda attenuation using vertical and horizontal recordings: after the onset of equipartition at 15 s from the origin time of the event the maps show identical anomalies. The data set comprises a selection of stations and waveforms used by De Siena *et al.* (2016) (available from PANGAEA Data Centre)

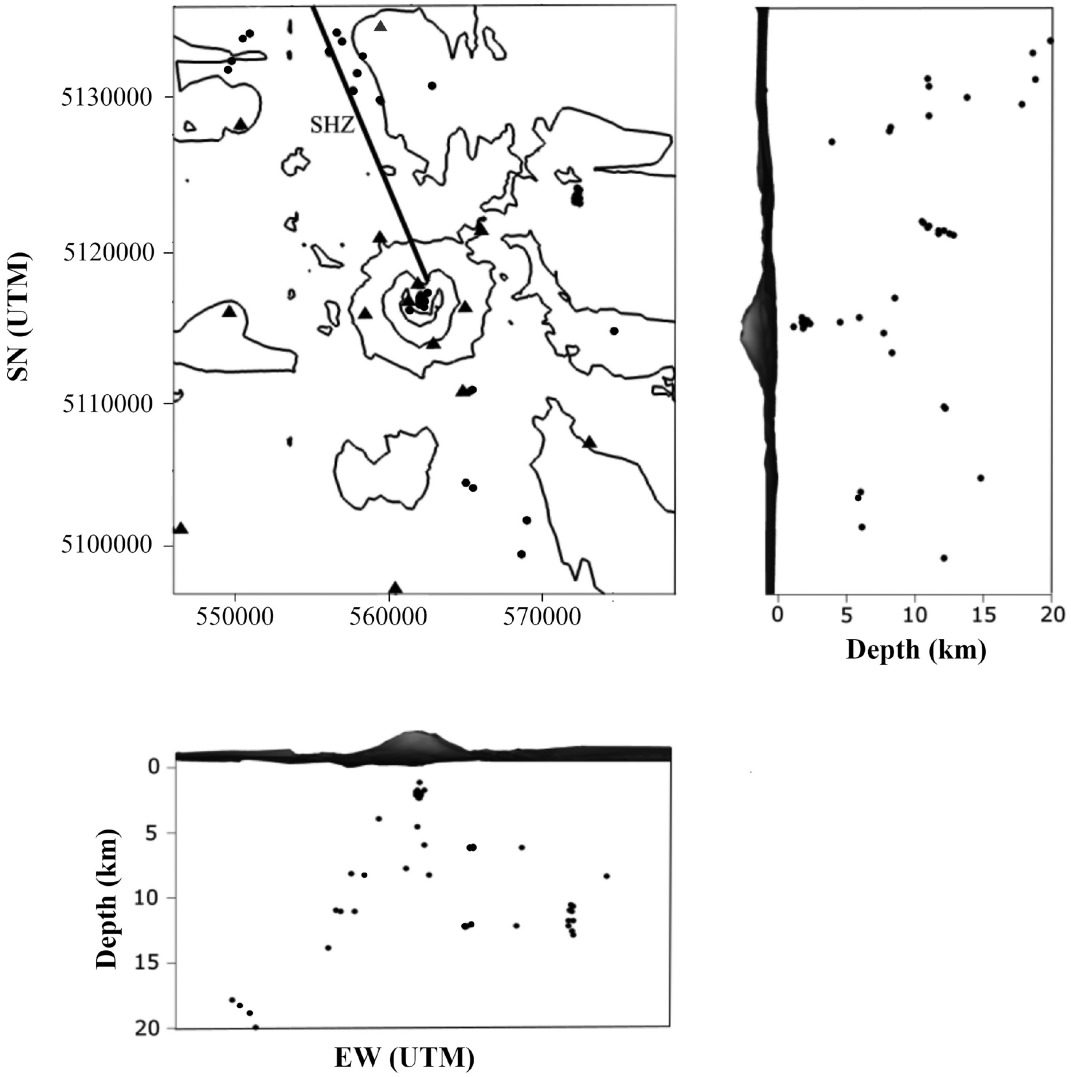

Figure 1. The earthquakes (black dots) and seismic stations (triangle) used in this study. The black line illustrates the St Helens Seismic Zone (SHZ).

to perform coda attenuation imaging with a line-regionalization approach, using the velocity model of Waite & Moran (2009) to obtain hypocentral distances and ray paths (Fig. 2). Seismic stations and earthquakes sample both the upper plumbing systems in the interval 0–20 km and the tectonic faults around it, as the SHZ (Fig. 1).

The seismic waveforms were filtered in four frequency bands, with central frequencies (f) of 3, 6, 12 and 18 Hz and bandwidths of one-third of the central frequency. Throughout the study, envelopes were computed with a Hilbert transform and smoothed with a moving window four times the inverse of the central frequency. The first step of the analysis consists in the application of the MLTWA technique, which will highlight frequency-dependent differences in the coda wavefield and provide input parameters to model coda intensities with the Energy Transport Equations (ETE). We build the attenuation kernels using a second analytic diffusive (AD) approximation (Del Pezzo *et al.* 2016) and compare the two spatial sensitivities. Finally, we discuss the inversion methods, specifically their resolution and stability for different inversion grids.

3.1 MLTWA

Two assumptions are necessary to apply the MLTWA technique: the direct S-wave dominates the early portion of an S-wave seismogram; the S-coda comprises scattered S waves. While in its first portion the S-wave amplitude is controlled by the total attenuation of the medium, coda waves are a product of scattering (Sato *et al.* 2012). We divided the filtered seismograms into three time-windows, starting from the S arrival. Picking the S waves is particularly difficult at short distances and inside the volcano; thus, we obtained the theoretical S-wave traveltime by multiplying the P-wave traveltime by a min and max Vp/Vs of 1.6 and 1.8. The calculated picking set the arrival if the operator picking was outside this interval. The time integrals $E_k(r)$ of the seismic energy density $E(r, t)$ in each window k is:

$$E_k(r) = \int_{t_k}^{t_k+\Delta t} E(r,t)\mathrm{d}t \quad k = 1...3, \tag{1}$$

where the energy is still a function of the source–station distance r. For each window we define the starting time t_k and we set the length to $\Delta t = 10$ s (Fig. 3). We express the wave energy decay for each cycle $-\Delta E/E$ in terms of the total quality factor parameter Q (related to the attenuation coefficient η) via the following equation:

$$-\frac{\Delta E}{E} = \frac{2\pi}{Q} = 2\pi\left(\frac{1}{Q_i} + \frac{1}{Q_s}\right) = \frac{\upsilon\eta}{f} \tag{2}$$

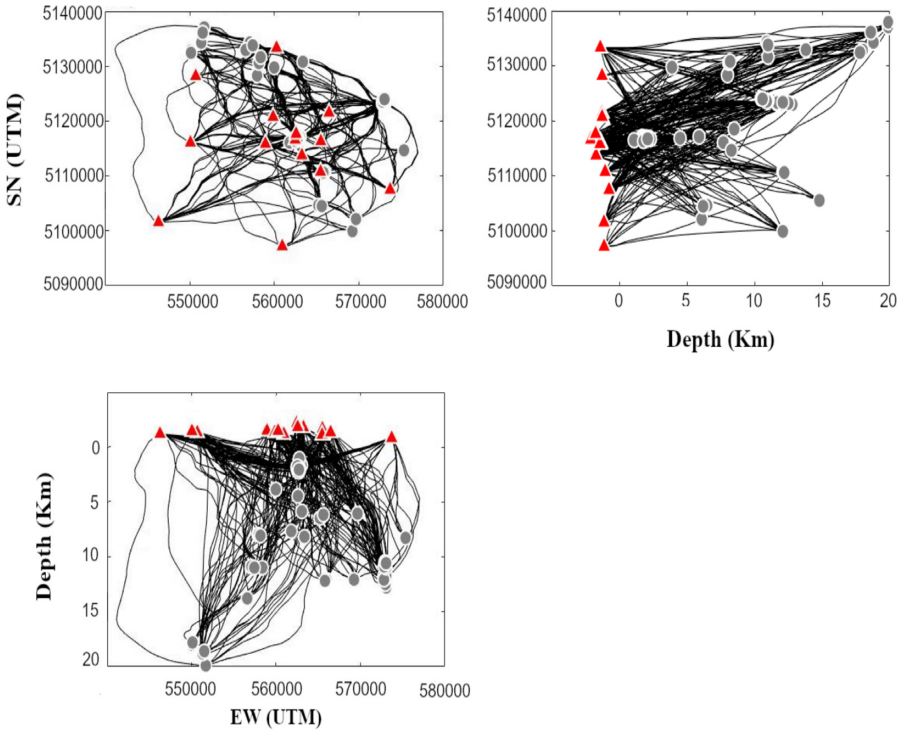

Figure 2. The earthquakes (grey dots) and seismic stations (red triangle) used in this study. The hypocentral distances are measured along rays computed in the velocity model of Waite & Moran (2009) by De Siena *et al.* (2014) using a ray-bending approach.

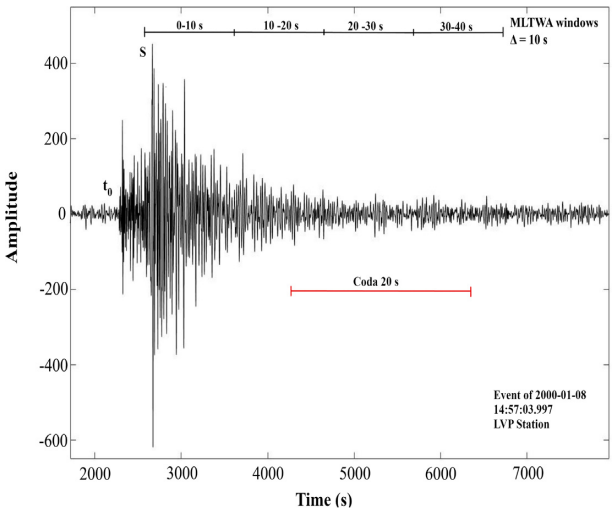

Figure 3. An earthquake registered at the station LVP on the 08/01/2000. The black lines above the seismogram show the 4 windows of 10 s used for the MLTWA. Coda waves recorded 20 s after the origin time (red line) are used in the kernel-based coda inversion.

where υ is the average wave speed, f is the frequency and Q_i and Q_s are absorption and scattering quality factor, respectively. The next step consists in the correction of the energy of each window $E_k(r)$ for both the geometrical spreading and the integral of the 10-s-long normalization window starting at $t_{\rm coda} = 40$ s from the origin time of the event: this procedure removes source and site effects (Mayeda *et al.* 1992):

$$E_k^{obs}(r) = \log_{10}\left(4\pi r^2 \frac{E_k(r)}{\int_{t_{coda}}^{t_{coda}+\Delta t} E_k(r,t)\mathrm{d}t}\right). \quad (3)$$

The resulting logarithms are plotted versus distance in the four frequency bands considered and fitted to the theoretical normalized energies (Fig. 4). The theoretical curves are modelled using the following L2-norm misfit function for a number of waveforms from i to N:

$$M(L_e^{-1}, B_0) = \sum_{i=1}^{N}\sum_{k=1}^{3}[E_k^{obs}(r_i) - E_k^{theo}(r_i, L_e^{-1}, B_0)]^2 \quad (4)$$

$E_k^{theo}(r_i, L_e^{-1}, B_0)$ is the theoretical normalized energy computed at distance r_i for the k-th time-window, fixing the L_e^{-1} and B_0 obtained from MLTWA. M is minimized with a grid search in the B_0 and L_e^{-1} parameter space, and the best-fitting values $\hat{L}_e^{-1}$ and $\hat{B}_0$ are given by the minima of the function. The isolines of the variable $M_{norm} = M(L_e^{-1}, B_0)/M(\hat{L}_e^{-1}, \hat{B}_0)$ give the error estimates on $\hat{L}_e^{-1}$ and $\hat{B}_0$. Being $M_{\rm norm}$ an F-variable (Del Pezzo & Bianco 2010), we estimated the model parameters using an F distribution (Pisconti *et al.* 2015), with a level of confidence higher than $F = 0.68$. The range of possible solutions for all the frequency bands obtained from the misfit function of eq. (4) are plotted in Fig. 5. For completeness we show the results obtained at short hypocentral distances and for the entire hypocentral range in Figs A1–A2.

3.2 Kernel-based forward model for coda imaging

Using passive seismicity at Mount St Helens, a multiple-scattering description of the scattering process is necessary (Del Pezzo *et al.* 2018). We adopt the Paasschens (1997) approximation of the Energy Transport Equation (ETE) solution in three dimensions to model the spatial sensitivity of coda-attenuation in space. The seismogram

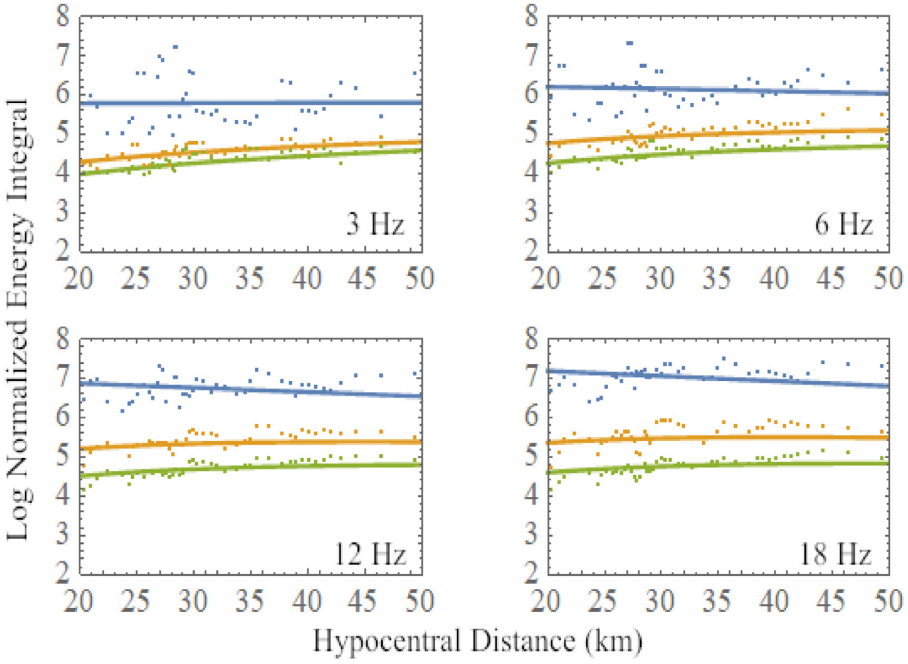

Figure 4. Plot of the normalized energy integral versus the hypocentral distance range of 20–50 km: blue, orange and green dots represent first, second and third window, respectively (Fig. 3), while the continuous lines are the best fit calculated with the solution of the transport equation in the uniform half-space assumption.

energy envelope is:

$$E^{3D}_{i,j}[r_{ij},t] \approx \frac{W_0 \exp\left[-Le^{-1}vt\right]}{4\pi r_{ij}^2 v}\delta\left[t-\frac{r_{ij}}{v}\right] + W_0 H\left[t-\frac{r_{ij}}{v}\right]\cdot \frac{\left(1-\frac{r_{ij}^2}{v^2t^2}\right)^{1/8}}{\left(\frac{4\pi vt}{3B_0Le^{-1}}\right)^{3/2}}\cdot \exp\left[-Le^{-1}vt\right] F\left[vtB_0Le^{-1}\left(1-\frac{r_{ij}^2}{v^2t^2}\right)^{3/4}\right], \quad (5)$$

where

$$F[x] = e^x\sqrt{1+2.026/x}$$

δ and H are the Dirac delta and the Heaviside step functions, respectively. Here, W_0 is the source energy, v is the seismic velocity (here, used a $v = 3.5$ km s^{-1}) and $r_{i,j}$ the 3-D source–station distance. Using the values of B_0 and Le^{-1} obtained with MLTWA and considering an average velocity, we can model both the multiple scattering and diffusive components of the theoretical energy envelope recorded at a given source–station distance (eq. 5). For our application, we are interested in the spatial sensitivity of the energy envelope at a given lapse-time (the half of the selected coda window), using the hypothesis of Pacheco & Snieder (2005):

$$K^{3D}_{i,j}[\varrho,t,B_0,Le^{-1},v] = \int_0^T E^{3D}[r_{s\varrho},\tau,B_0,Le^{-1},v] \times E^{3D}[r_{\varrho r},T-\tau,B_0,Le^{-1},v]\mathrm{d}\tau, \quad (6)$$

where ϱ is the space point with coordinates $\{i,j,z\}$, $r_{s\varrho}$ is the point-to-source distance, $r_{\varrho r}$ is the point-to-receiver distance, T the lapse time and τ the integration variable.

The solution is implemented in Del Pezzo *et al.* (2018) by convolution of the coherent (first) and multiple scattering (second) terms in eq. (5) across an extended grid comprising the medium (Fig. 6).

To provide a kernel value at the poles at source and station locations, we linearly interpolate the kernels using the nearest eight nodes. The total energy loss at the station (which always shows the highest sensitivity) normalizes the contribution to the energy loss at each node of a 2-km-spaced 3-D grid. However, we need to obtain 2-D spatial variations, as (1) the limited array coverage in the period would not allow solving a large 3-D inversion problem for the spatial absorption and (2) we could not compare the maps with the 2-D line-regionalization approach followed by De Siena *et al.* (2016), or with the results of the 2-D analytic diffusive approximation. Thus, for each source–station pair, we down-scaled the 3-D sensitivity to 2-D by averaging on each depth column and then normalizing for the total weight of the source–station pair. The procedure is similar to that followed by De Siena *et al.* (2016) to downscale their 3-D ray-dependent sensitivities to 2-D, but is now applied to 3-D kernels. In Fig. 7(left-hand panel, the 2-D ETE kernels at 3 and 18 Hz are computed from the 3-D kernels (Fig. 6).

The ETE kernels are then compared in the same figure with the 2-D kernels obtained assuming an analytic diffusive approximation (AD - right, Del Pezzo *et al.* 2016):

$$f[x,y,x_r,y_r,x_s,y_s] = \frac{1}{4\pi\delta_x D^2\delta_y} \times \exp\left[-\left(\frac{\left(x-\frac{x_r+x_s}{2}\right)^2}{2(\delta_x D)^2}+\frac{\left(y-\frac{y_r+y_s}{2}\right)^2}{0.5(\delta_y D)^2}\right)\right] + \frac{1}{2\pi\delta_x D^2\delta_y}\exp\left[-\left(\frac{(x-x_s)^2}{2(\delta_x D)^2}+\frac{(y-y_s)^2}{2(\delta_y D)^2}\right)\right] + \frac{1}{2\pi\delta_x D^2\delta_y}\exp\left[-\left(\frac{(x-x_r)^2}{2(\delta_x D)^2}+\frac{(y-y_r)^2}{2(\delta_y D)^2}\right)\right]. \quad (7)$$

Here, D is the source–station distance, x and y the spatial coordinates, $[x_r, y_r]$ the station coordinates and $[x_s, y_s]$ the source

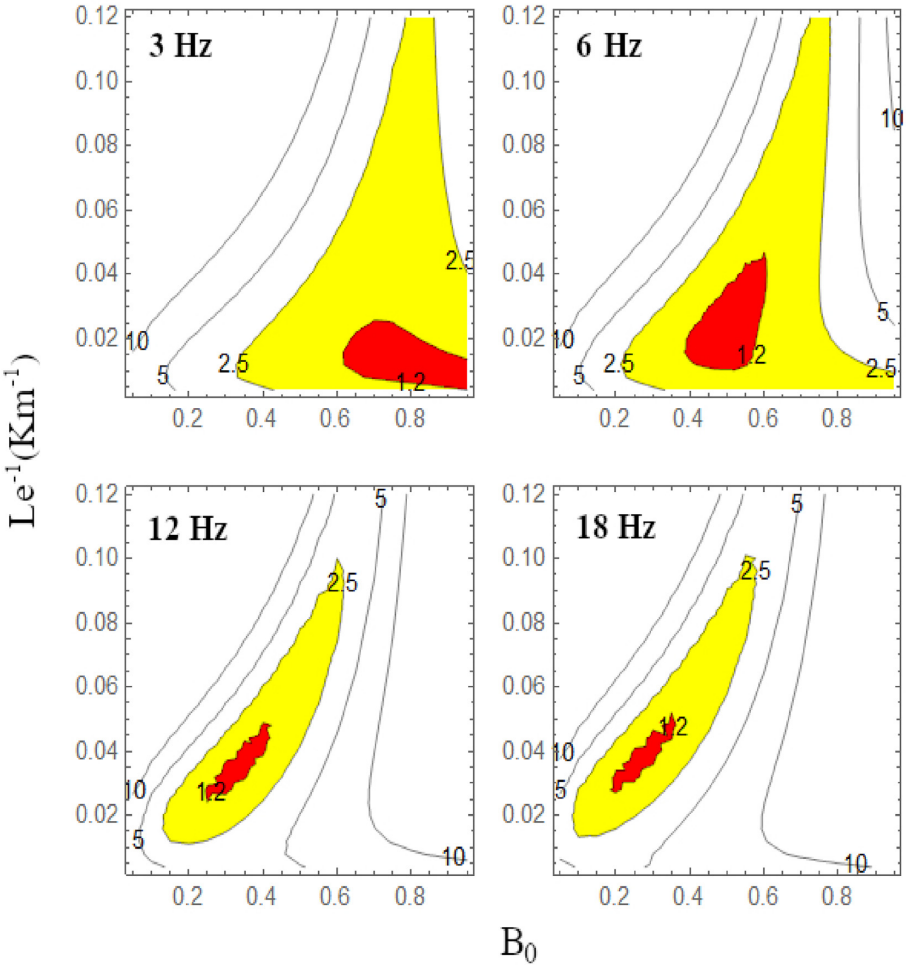

Figure 5. Gaussian error distribution associated to the MLTWA estimates at 68 per cent (red), 95 per cent (yellow) and 99 per cent (white) at each frequency.

coordinates. δx and δy are the spatial aperture of the weighting function. The AD kernel is effective at reconstructing shallow (<4 km depth) 2-D (Del Pezzo *et al.* 2016; De Siena *et al.* 2017) volcanic structures using data from active and passive surveys; however, Del Pezzo *et al.* (2018) show that this diffusive approximation does not give a satisfactory fit when using passive data sampling both the plumbing system of the volcano and crustal areas around it. The difference between the AD and the ETE kernels (Fig. 8) highlights the increased sensitivity of the ETE kernels far from source and receiver at the expenses of the source-receiver connection.

3.3 Kernel-based coda inversion

The waveforms used in the inversion for the spatial distribution of coda attenuation are filtered in the same frequency bands of the MLTWA (3, 6, 12 and 18 Hz). The envelopes are then computed and cut from a lapse time of 20 s in a time window of length 20 s (Fig. 3). We obtain Q^{-1} at each node using a first-order Tikhonov inversion approach.

3.3.1 AD inversion

The L-curve, the log–log plot of the norm of the regularized solution versus the norm of the corresponding residual norm, is used to assess the best smoothing parameter for the AD inversion (0.09 as shown in Fig. A3, in the Supporting Information). We also selected other parameters to test the resolution and stability of the model (0.009 and 0.26, Fig. A3) and we performed the corresponding checkerboard tests at various node spacing (Fig. 9). With a damping factor of 0.009, anomalies are well recovered in the centre of the model, but artefacts appear due to poor ray coverage elsewhere (Fig. A4, in the Supporting Information). The value of 0.26 shows very few anomalies and looks overdamped (Fig. A5, in the Supporting Information). The value of 0.09 gave a good compromise between the resolution, stability, and effective reconstruction of anomalies for different inputs (Fig. 9).

3.3.2 ETE inversion

The L-curve obtained using the ETE kernels (Fig. A6, in the Supporting Information) shows that the inversion problem for Q_c^{-1} is less constrained than for the AD inversion. The checkerboard test has been performed for the ETE kernels using damping parameters of 0.007, 0.07 and 0.7 (Fig. 10). Only a lower damping value (0.007, left-hand panel) gives sufficient resolution on large-scale anomalies across the area, while the other values can only resolve an anomaly under the volcanic edifice. The L-curve and checkerboard tests prove that the ETE solution is neither resolved nor stable, differently from the AD solution if we choose similar damping values (compare Fig. A6 and Fig. A3 in the Supporting Information).

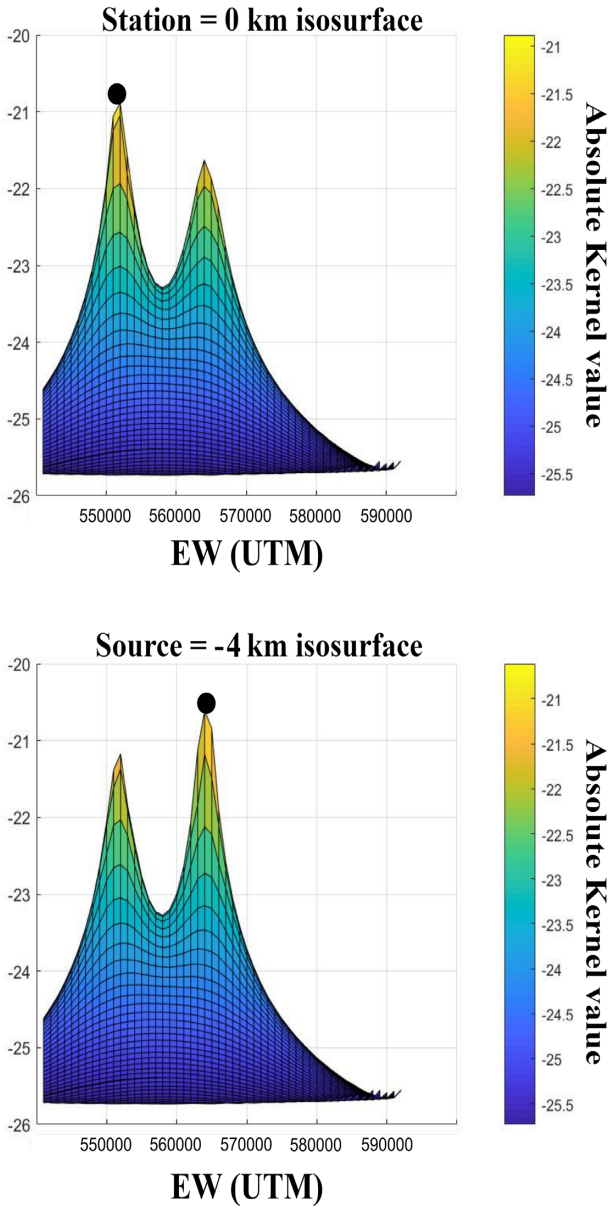

Figure 6. Two isosurfaces showing an absolute kernel at 0 km (upper panel) and 4 km (lower) depths. Station and source locations are shown in the top and bottom panels, respectively. The colourbars represent the argument of the exponent of the kernel value.

4 FORWARD MODELLING WITH RADIATIVE3D

Both MLTWA and sensitivity kernels rely on the assumption of bulk sensitivity (no surface wave enhancement) in a half-space. They both assume no vertical or horizontal variations in the scattering properties of the medium. We test these hypotheses simulating vertical earthquake recordings for two earthquakes and two stations (Fig. 11a) and for the 3 and 12 Hz frequency bands. The far-field event (**F** -red dot) nucleates at 19.9 km depth as a strike-slip event (Brocher *et al.* 2017). Event **N** is a strike-slip source with hypocentre below the central crater at a depth of 2 km (Lehto *et al.* 2013). Fig. 11 shows the seismograms recorded at SHW (on the western side of the volcano – elevation 1.45 km) and YEL (at the top of the debris avalanche inside the crater – elevation 1.75 km): the stations are at the same epicentral distances in the far field and are affected by approximately the same radiation pattern. In the near-source case, we correct amplitudes for the geometrical spreading difference between SHW and YEL but do not remove the differences in radiation patterns.

At both 3 and 12 Hz we forward model the envelopes in the far (Fig. 11, F) and near (N) fields at both stations using RADIATIVE3D. We set up two half-space model with average crustal parameters: the crustal low-scattering model (LS) and the high-scattering model (HS). The parameters used here are not unique, as demonstrated by Przybilla *et al.* (2009) and recently confirmed by Cormier & Sanborn (2019): any combination having constant $\frac{\epsilon^2}{a}$ could produce the same amount of scattering, leading, for example, to similar delays of the *S*-wave peak. The envelope of a Ricker wavelet with central frequency 10 Hz is convolved to the radiative transfer envelopes after the simulation. Our scope is to test if a half-space model with no interfaces fits envelopes at all stations and frequencies, both for the MLTWA and the late lapse-times chosen for the tomographic inversion. We report the wavelengths (λ) corresponding to the LS and HS models in the panels showing observations in the far field (Fig. 11b) and near field (Fig. 11c), respectively. The transport mean free paths and times (TMFP and TMFT) obtained for the best-fitting model are shown on each seismogram. In Fig. 11(b) we report TMFP and TMFT at 3 Hz for station SHW, as the LS model better fits early coda while the HS model performs better at late lapse times. In each simulation we use a total of 140 millions particles to stabilize the solutions (Sanborn *et al.* 2017). At 3 Hz, the near-field wavelength at YEL ($\lambda = 0.6$) is of the order of the propagation distance (3.8 km).

5 RESULTS AND DISCUSSION

5.1 MLTWA results and correlations with other volcanic areas

The normalized energy integral results were used across three different ranges of hypocentral distances: 0–20 km, 0–50 km and 20–50 km. Fig. 4 shows the behaviour of the three different time windows in the four frequency bands for the distance range of 20–50 km. Although we try to fit the coherent part (blue line) with a single layer model, it is evident that at least two scattering regimes act on our data: the short range scattering (Fig. A1 in the Supporting Information) for waveforms nucleated in the central plumbing system, and the long range scattering (Fig. 4), characterizing waveforms produced across the deep tectonic faults surrounding the volcano, as the SHZ. This separation is similar to that observed at Mt Fuji volcano using a much wider data set (Chung *et al.* 2009). In the short-range regime, no acceptable fit can be obtained for the coherent wave at all the frequencies and the solution for the remaining two windows collapses to a single one: the wavefield inside the volcanic cone is apparently diffusive at very short lapse times (Wegler & Lühr 2001). At lower frequencies (3–6 Hz) the first window always shows higher data variations than the other two windows in all the ranges, a typical result in MLTWA analyses (Mayeda *et al.* 1992; Pisconti *et al.* 2015; Del Pezzo *et al.* 2011). We infer that this is a radiation pattern effect, most significant in the part of the seismogram where the *S*-wave arrival dominates.

The MLTWA results in the 20–50 km range show the best fits and revealed a predominance of scattering attenuation versus absorption in the MSH area at low frequency: the seismic albedo B_0 is higher or equal than 0.5 in the 3 and 6 Hz frequency bands (Table 1), a typical

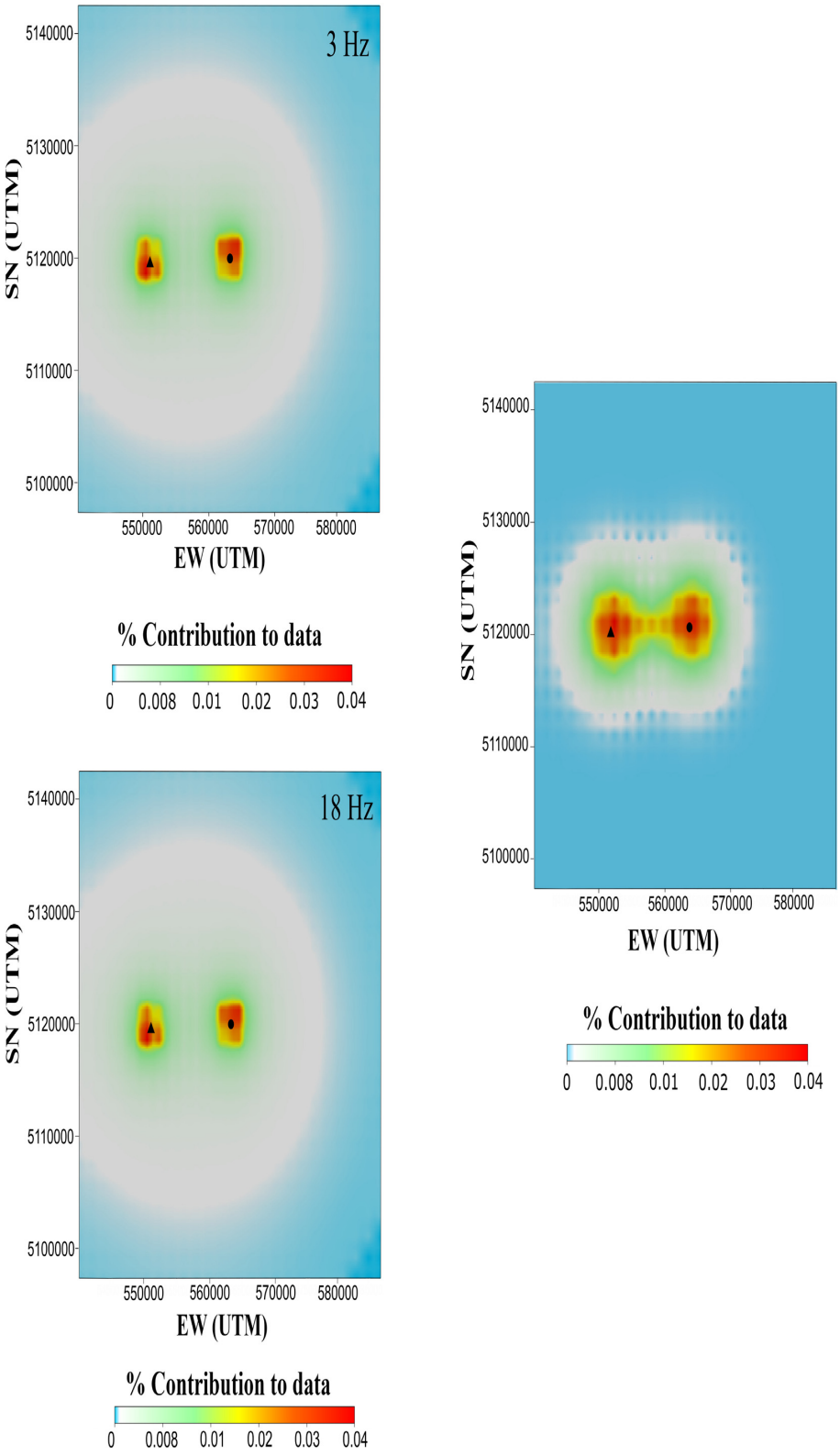

Figure 7. Comparison between normalized 2-D ETE kernels for a single source–station pair (left-hand panel, top: 3Hz and left-hand panel, bottom: 18 Hz) and AD kernels (right-hand panel). Kernel functions are represented as the percentage contribution of each node to Q^{-1} for a single source–station pair. Source and receiver are represented by a black dot and a triangle, respectively.

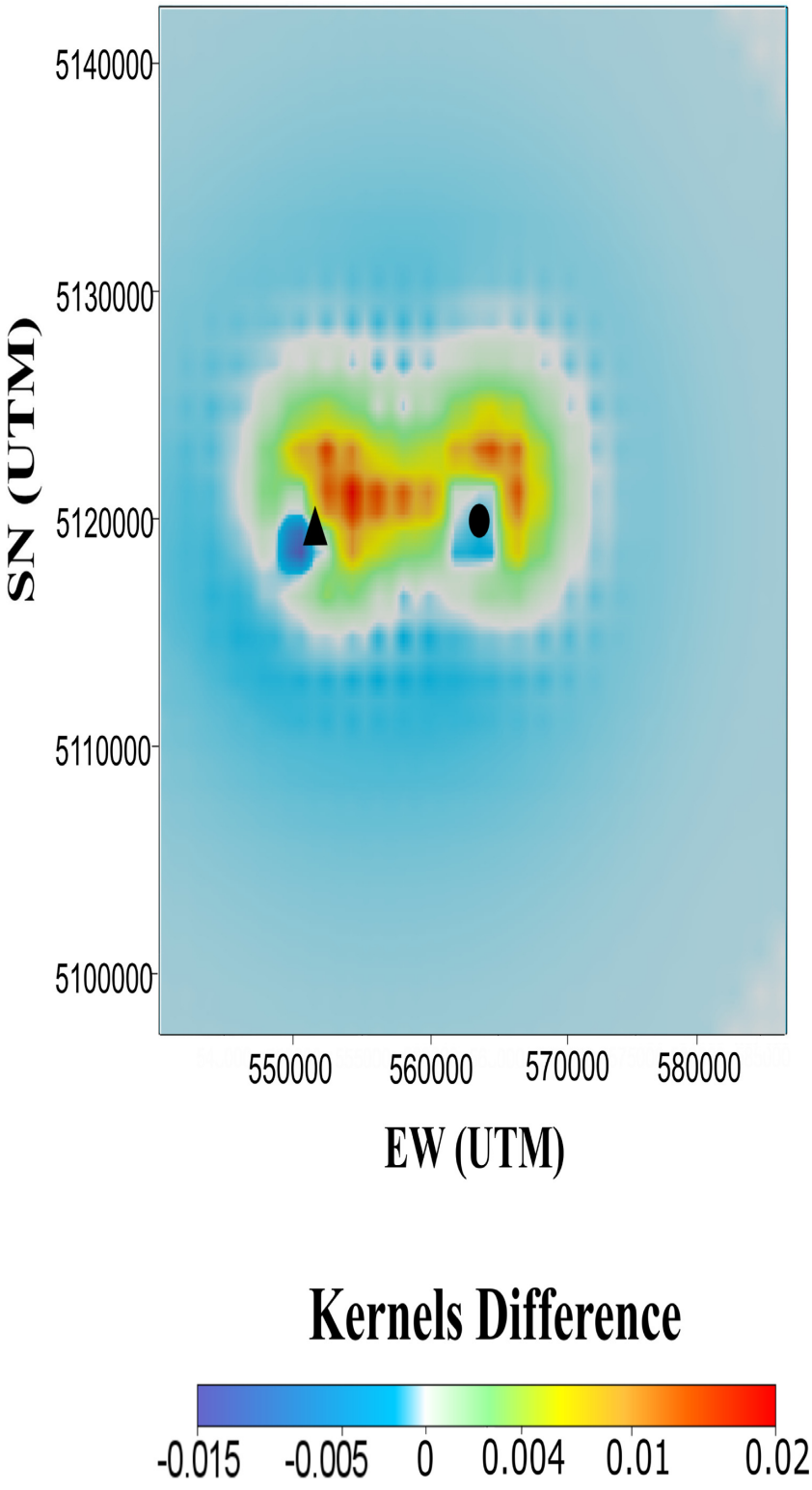

Figure 8. Difference between the AD kernels and the 2-D ETE approximation at 3 Hz. In blue (negative), the ETE kernels show a higher sensitivity than the AD, while, in red (positive), the sensitivity is higher for the AD.

result in volcanic areas (Ugalde *et al.* 2010; Prudencio *et al.* 2013b, 2017; Del Pezzo *et al.* 2019). As $L_e^{-1} = \eta_i + \eta_s$, $B_0 = \eta_s / L_e^{-1}$ and $\eta_{(s,\,i)} = 2\pi f / v Q_{(s,\,i)}$, we derived the values of Q_s^{-1} and Q_i^{-1} for MSH.

The results of the MLTWA (Table 1) show (1) a decrease in scattering attenuation (Q_s^{-1}) and (2) a constant absorption with increasing frequency. Open-conduit, active and dormant volcanoes mostly show a similar decreasing scattering behaviour with increasing fre-

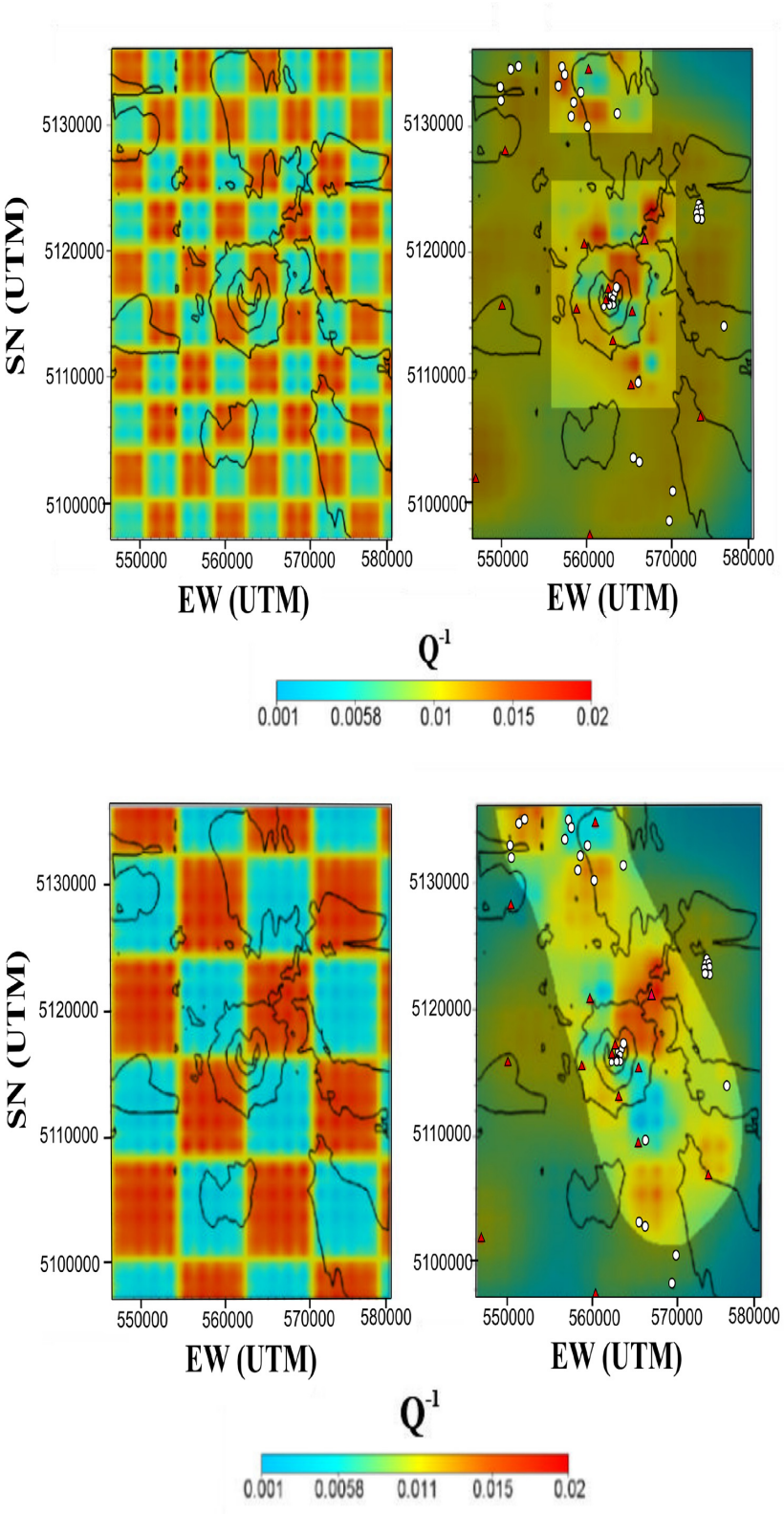

Figure 9. Checkerboard tests for the AD kernels performed using 4 x 4 km (top panel) and 8 x 8 km (bottom panel) anomalies as input. The test is solved at 3 Hz over a 2 x 2 km spaced regular grid with a damping parameter of 0.09. A grey mask covers the unresolved anomalies.

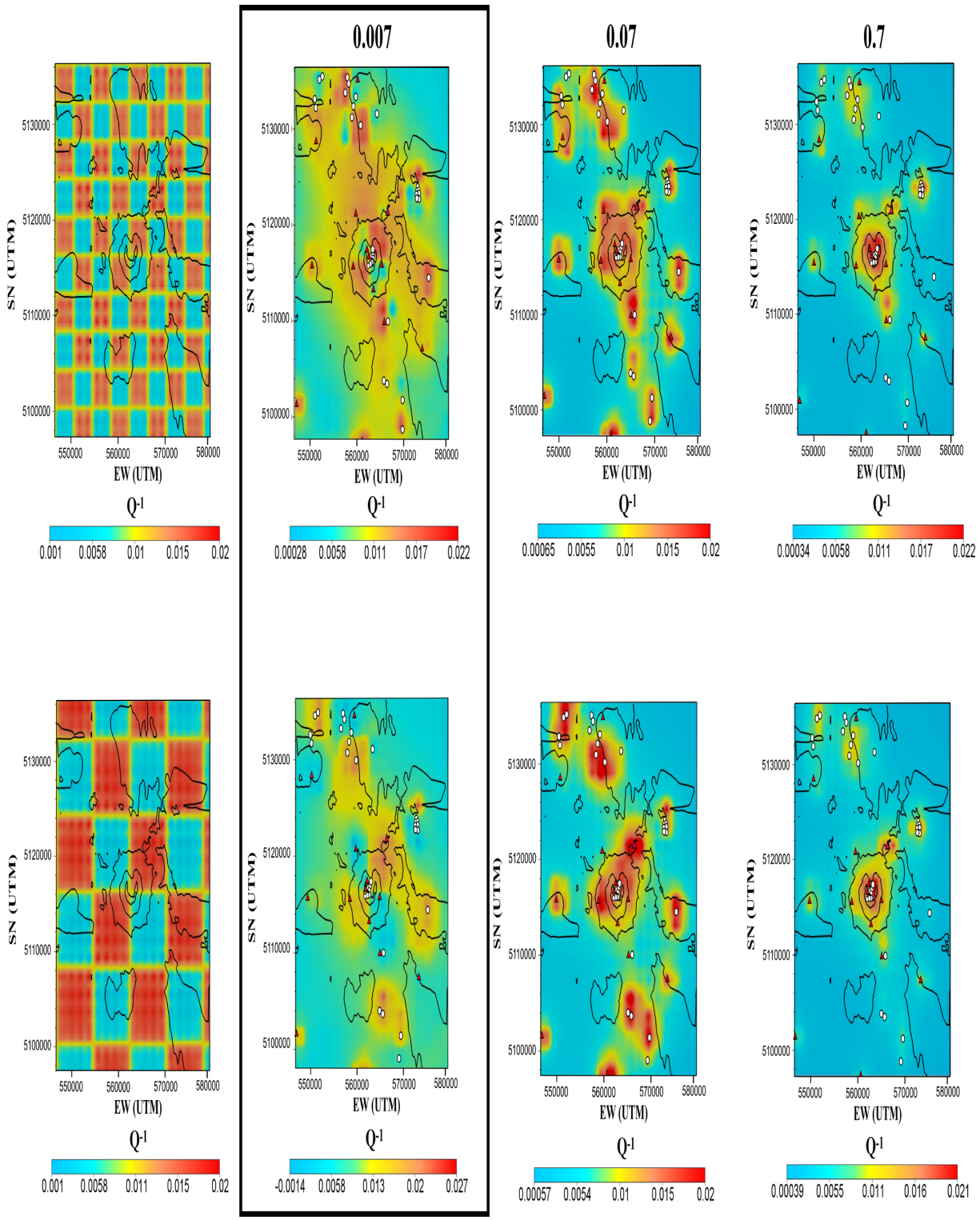

Figure 10. Checkerboard test with 4 x 4 km (upper panel) and 8 x 8 km (lower) anomalies as input, for the ETE kernels using different damping parameters (left-hand panel: 0.007; centre panel: 0.07; right-hand panel: 0.7). The seismicity (white dots) and stations (reds triangle) are plotted on all the output results. In the black square, the value of 0.007 considered for the imaging.

quency (e.g. Del Pezzo *et al.* 2019). However, intrinsic attenuation is one order of magnitude lower at dormant or inactive volcanoes, like Mt Vesuvius (Bianco *et al.* 1999) and Mt Fuji (Chung *et al.* 2009), then in active ones. By comparing the obtained Q_i^{-1} and Q_s^{-1} at all frequencies we confirm an agreement with the results obtained at Fuji volcano. At least in its pre-eruptive stage (until November 2003), Mount St Helens thus behaves as expected for an andesitic volcano in a tectonic setting, with relatively low amount of molten materials in the plumbing systems. Nevertheless, at the pre-eruptive Mount St Helens, the seismic albedo (B_0) is consistently

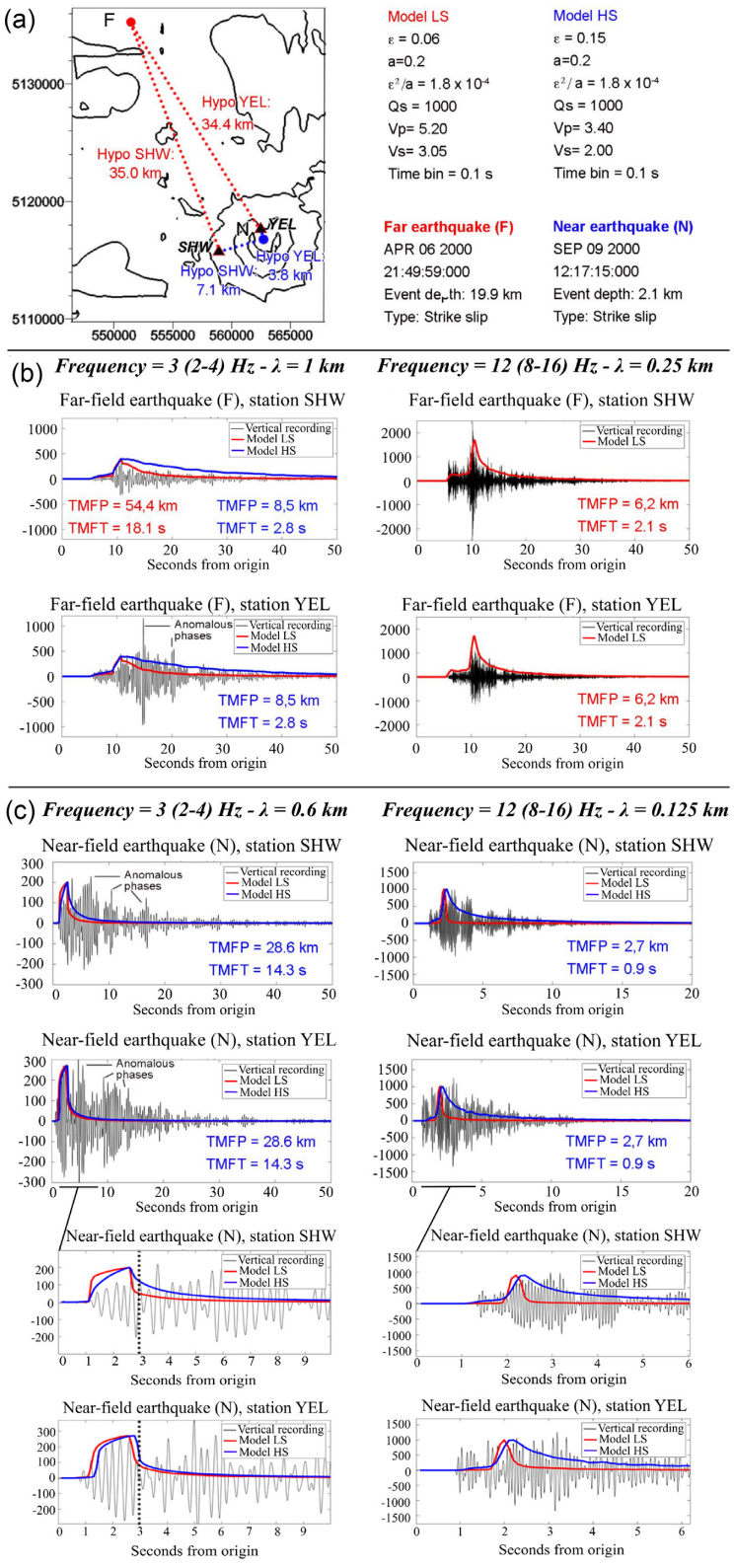

Figure 11. Radiative transfer model of far (F) and near (N) fields recordings at stations SHW and YEL. (a) Earthquakes characteristics and two models (LS and HS) used to reproduce seismogram envelopes. (b) Far-field recordings and envelope models at 3 Hz (left-hand panel) and 12 Hz (right-hand panel). On each panel we report the Transport mean free path (TMFP) and the Transport mean free time (TMFT) of the best-fitting model. (c) Same as panel b in the near-field recordings. The lowermost panels a zoom on the direct wave and early coda. The dotted vertical line (left-hand lowermost panel) marks the onset of surface waves scattering at 3 Hz.

Table 1. MLTWA results in the 20–50 km range.

Frequency (Hz)	B_0	Le (km)	η_i	η_s	Q_i^{-1}	Q_s^{-1}
3	0.95 ±5%	125.0 ±100%	0.0004 ±100%	0.0076 ±4%	0.0007 ±19%	0.0014 ±2%
6	0.50 ±20%	41.6 ±66%	0.0120 ±81%	0.0120 ±48%	0.0011 ±8%	0.0011 ±4%
12	0.35 ±10%	27.8 ±38%	0.0234 ±62%	0.0126 ±50%	0.0011 ±3%	0.0005 ±2%
18	0.25 ±60%	27.8 ±38%	0.0270 ±100%	0.009 ±100%	0.0008 ±3%	0.0002 ±6%

higher than at Mt Fuji at all frequencies. At 3 Hz $B_0 = 0.95$ as never observed in other volcanic settings. This result will be interpreted in the following sections.

5.2 The trigger of anomalous scattering at 3 Hz

Our scope in this section is to assess the reliability of the assumptions behind MLTWA and the diffusive sensitivity kernels. At 12 Hz, the low-scattering model (Model LS in Fig. 11b, right-hand panel, red line) satisfactorily fits intermediate and late coda envelopes in the far-field. The coda decay is almost identical at the two stations after 20 s, corresponding to about ten times the computed transport mean free time (TMFT). Nevertheless, the data recorded at YEL show a much wider broadening and dissipation of the coherent wave: while the last phenomenon is consistent with forward scattering along the source–station path, the broadening is more likely due to near-receiver scattering at YEL, causing coupling of body and surface waves (Larose *et al.* 2005b). This effect is enhanced at 3 Hz (Fig. 11b, left-hand panel): the LS Model correctly reproduces the direct arrival and early coda at station SHW but higher amplitudes than expected appear in the late coda. The HS model is necessary to fully reproduce the 3 Hz envelope at station YEL: significant anomalous phases now appear in the intermediate coda, dominating the envelope and breaking the assumptions behind MLTWA. Our hypothesis is that the shallow plumbing system, the crater and the debris avalanche of the 1980 eruption immediately act as near-station scatterers for far-field observations at YEL. The enhancement of scattered surface waves is especially efficient at 3 Hz (wavelength of 1 km or less) as scatterers will be located in the first half wavelength from surface (Larose *et al.* 2005b).

We get more insight into the scattering processes using the recordings of the near-field event (N - Fig. 11c), where the high-scattering model better fits 12 Hz *S*-wave coda envelopes (blue line) at late lapse times. We zoom on the 0–6 s time interval at 12 Hz to highlight differences in early and intermediate coda (lowermost right-hand panel): here, anomalous phases similar to those observed at 3 Hz in the far-field play a significant role in the late coda, dominating intermediate coda envelopes at both stations. These time spans are not satisfactorily recovered by our model, likely because both source and receivers are embedded in the high scattering medium, where scatterers across the entire depth span can equally enhance surface wave sensitivity (Larose *et al.* 2005b; Obermann *et al.* 2013). Fig. 11c (left-hand panel) shows that no fit is achievable at 3 Hz for the whole envelope. The models predict quite well the direct wave envelope (see zoom in the lowermost left-hand panel) but surface waves with anomalous phases similar to those observed in the far field now dominate the envelope after 3 s (dotted line), with a measured velocity of 1.775 km s^{-1} (the *S*-wave velocity is 2 m s^{-1}).

These results confirm the likely role of shallow unconsolidated materials in biasing coda data at 3 Hz. When the wavelength is of the order of the propagation distance, like in the near field , surface waves dominate the coda envelopes. The effect decreases but is still present at higher frequencies, where the HS model only apparently fits late *S*-coda, especially at YEL (Fig. 11c). The results of MLTWA are thus likely unreliable in the near field under the volcano as scattering is too strong to detect any coherent wave produced inside the volcanic edifice (Wegler 2003; King *et al.* 2017). This scattering affects the assumption behind MLTWA and produces the low fit of the coherent wave with the model at all distances (Figures A1–A2). The effect is so extreme at short source–station distances that no coherent energy can be recognized (Fig. A1). Such biases appear in MLTWA applications of other volcanic areas at the regional scale, like those at Mt Etna (Del Pezzo *et al.* 2019). Differences in scattering characteristics between 3 Hz and higher frequencies are reported in several coda-attenuation imaging studies of volcanoes, especially in the presence of a volcanic edifice (e.g. Tramelli *et al.* 2009). Nevertheless, an albedo as high as 0.95 had never been measured in volcanoes. We infer that this result is indicative of the biases that the higher scattering in the plumbing system and volumes under the debris avalanche will produce on any coda-attenuation imaging when using bulk sensitivity kernels or regionalization.

5.3 Reliability of coda-attenuation kernel imaging in volcanoes

The AD kernel functions of Del Pezzo *et al.* (2016) can be applied in a medium where the scattering coefficient η_s falls between 0.04 and 0.8—indicative of the presence of a diffusive (bulk) wavefield. The values obtained by the MLTWA fall below it at all the frequencies, but are particularly far from the interval at 3 and 18 Hz. While 18 Hz data could be too attenuated to produce valid results at the chosen lapse times, this is not certainly the case at 3 Hz. The ETE kernels are computed in 3-D for each source–station pair (Fig. 7, left-hand panel). They hypothesize bulk sensitivity only (Obermann *et al.* 2013) and use the albedo and extinction lengths measured via MLTWA as input. These inputs produce no appreciable difference in sensitivity at different frequencies (Fig. 7, left-hand panel). Both the AD and ETE kernels show the highest sensitivity around the station and source locations but only the AD kernels have consistent sensitivity between the two. By comparing the checkerboard tests and testing stability in the two cases (Figs 9–10 and A3–A6), we observe that, while a diffusive kernel models scattering propagation incorrectly for deeper earthquakes, an ETE kernel provides less focus on structures between source and receiver. The AD kernels thus overestimate the sensitivity of coda measurements, artificially improving their coverage. The ETE solution is representative of the true bulk multiple-scattering process; however, once data are inverted, the ETE solution is less stable. In previous section we observed that near-receiver scattering enhancing surface waves is a factor biasing imaging also in the far field. The high-attenuation and high-scattering body imaged by De Siena *et al.* (2016) and recognized as part of the debris avalanche of the 1980 eruption remains the predominant anomaly in our 3 Hz kernel-based images, even if shifted about 2 km east (Figs 12 – top left and 13). We remind that 2 km is our model parametrization. In the far-field,

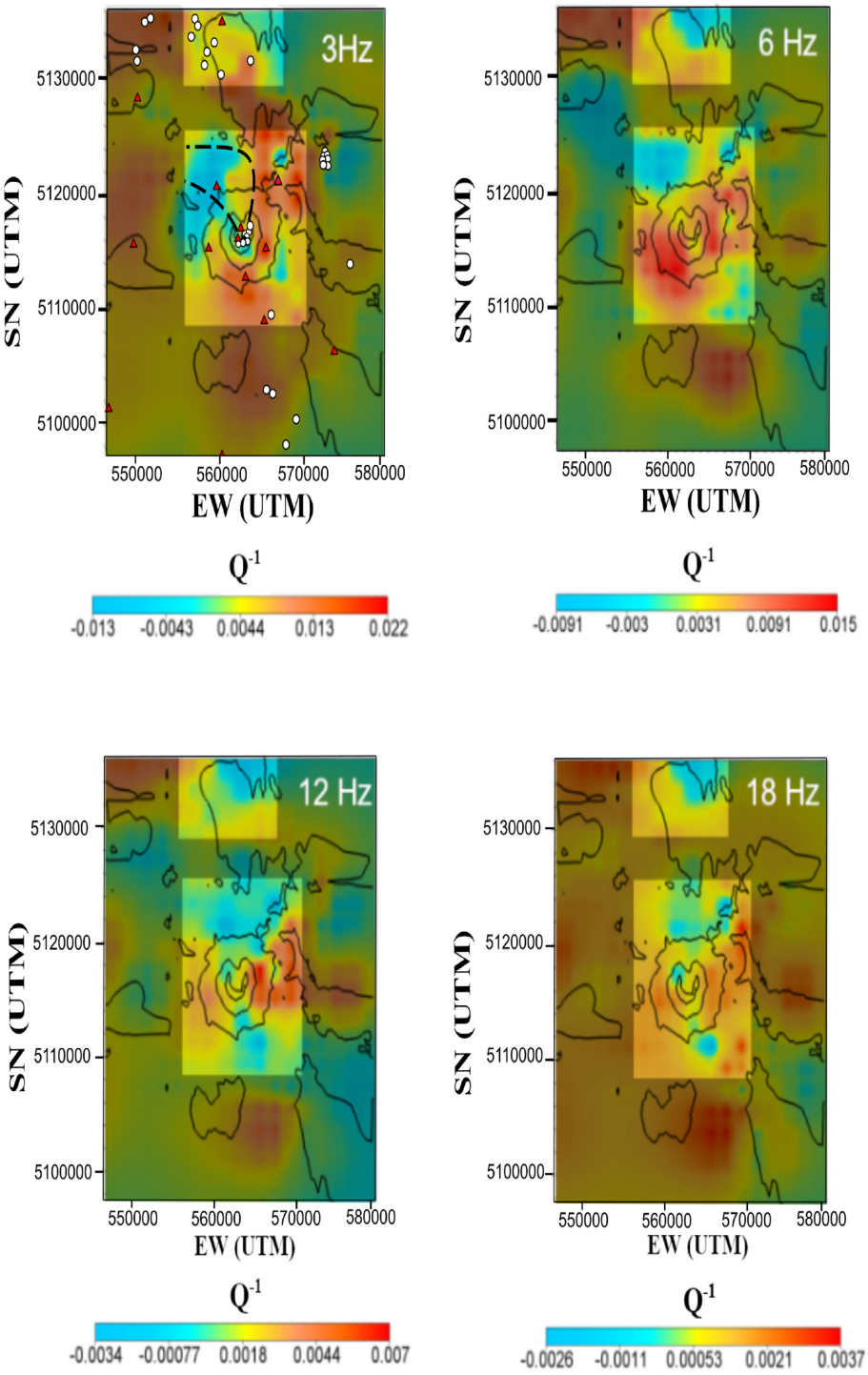

Figure 12. Coda attenuation mapping using the AD kernels with a damping parameter of 0.09, at 3, 6, 12 and 18 Hz. Events (white dots) and stations (red triangles) are plotted on the 3 Hz image. The black dashed line outlines of the debris avalanche of 1980 in our area of interest, at 3 Hz.

a high-scattering half-space model seems sufficient to model late-coda features on the debris avalanche and in the crater at 3 Hz; however, we conclude that coda waves are not anymore in the bulk at stations located near or on shallow unconsolidated materials, contradicting the hypothesis behind the application of the sensitivity kernels.

Higher frequencies (12 Hz), which are mainly comprised of body waves (Galluzzo *et al.* 2015) and fulfill the half-space approximation, are necessary to scan the interior of the volcano with the proposed kernels. Considering the uncertainties on the MLTWA results, η_s falls in the diffusive range at 6 and 12 Hz (Del Pezzo *et al.* 2016). The results of the forward modelling confirm that the

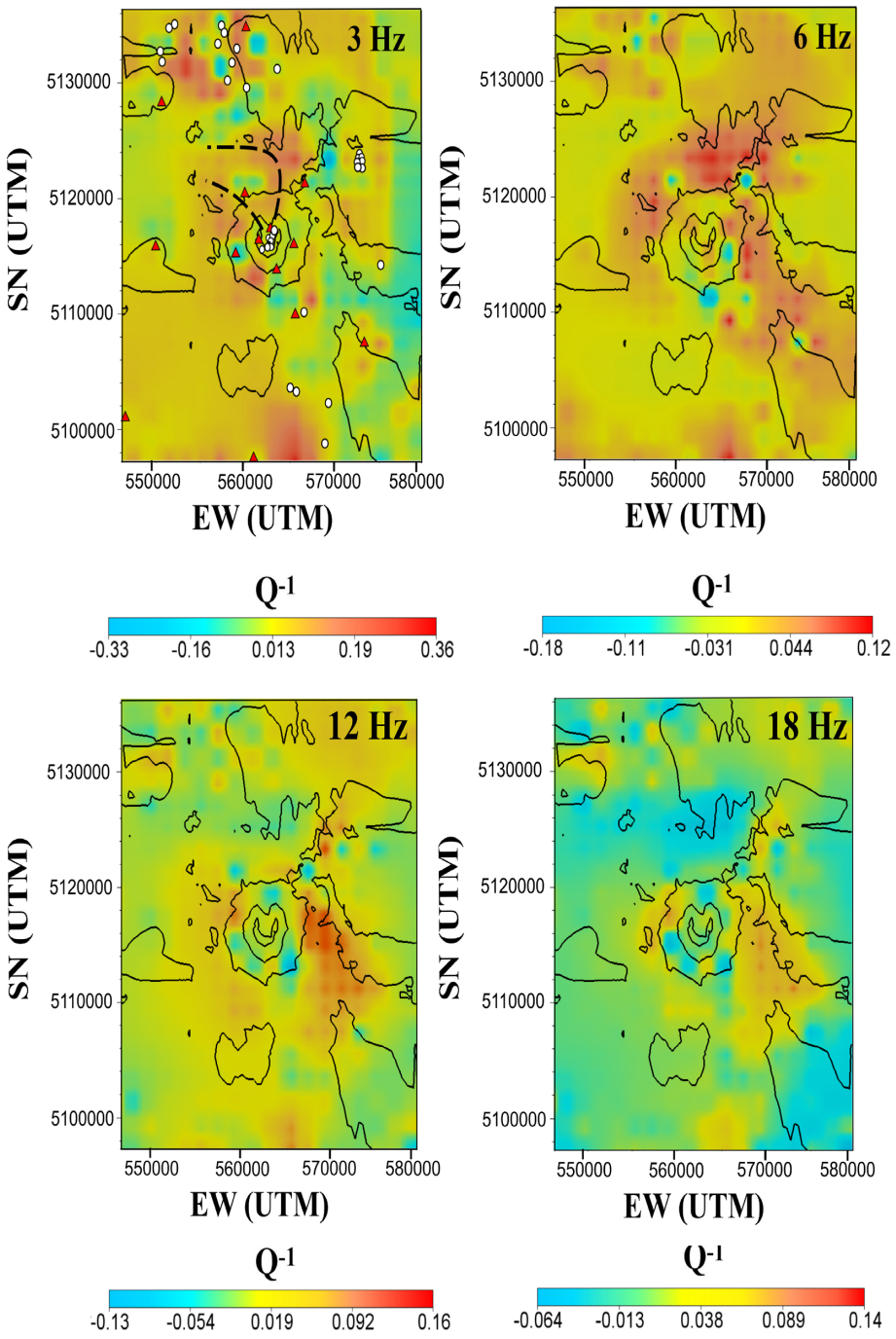

Figure 13. Coda attenuation mapping using the ETE kernels and a damping parameter of 0.007 at 3, 6, 12 and 18 Hz. Events (white dots) and stations (red triangles) are plotted on the 3 Hz image. The black dashed line outlines of the debris avalanche of 1980 in our area of interest, at 3 Hz.

transport mean free path is sufficiently small to apply the diffusive kernels after $t = 20$ s ($t \gg$ TMFP, Fig. 11), if signal is present. An equipartition test for an event nucleated in 2005 far from the volcano (Fig. 14, previously no horizontal components were available) shows that this necessary condition for the use of a diffusive approximation is satisfied after 20 s. Considering the mentioned instability of the 3 Hz frequency band, we plot the energy ratio H^2/V^2 against time after filtering between 4 and 18 Hz following Hennino *et al.* (2001). We can note how the ratio stabilizes after 20 s from the origin time and for 60 s, even if at values lower than 1.

We thus interpret the results of the imaging with AD and ETE kernels at 6 and 12 Hz in terms of deep structures. Both tomographic models (Figs 12 and 13) show the progressive shift of a high attenuation anomaly from the debris avalanche and southern portions of the volcano (6 Hz) to its eastern side (12 Hz). The anomaly at 12 Hz is consistent with the shift of the deep plumbing materials towards the east imaged by previous studies (De Siena *et al.* 2016; Kiser *et al.* 2016, 2018). The results of the 4-km-spaced checkerboard test (Fig. 9) demonstrate that, in a diffusive approximation, we can resolve such an extended anomaly. While a much wider data set is necessary to remove tomographic biases, the silver lining

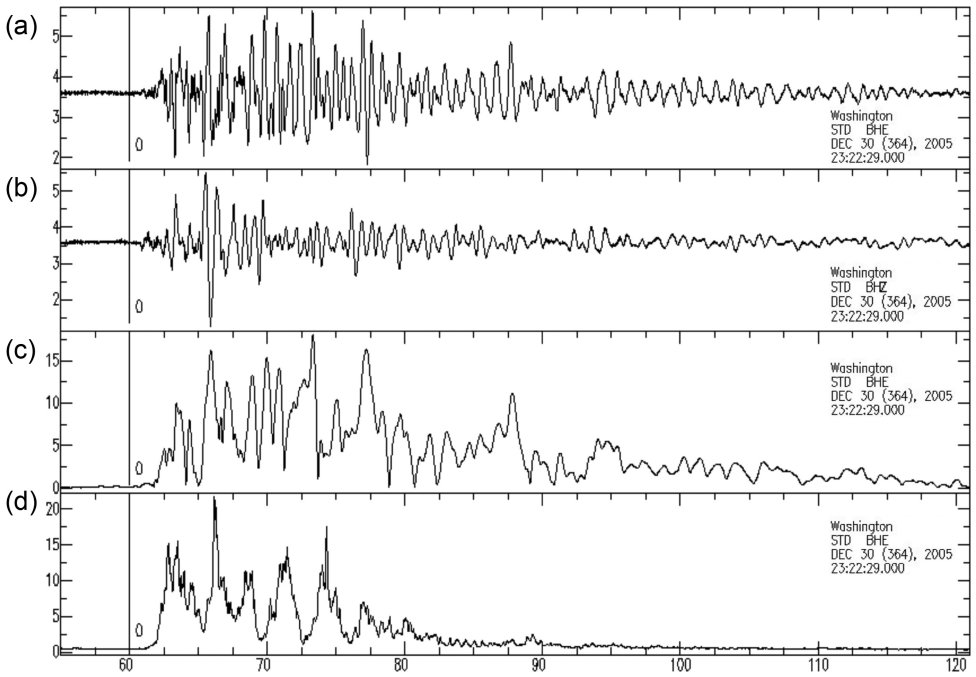

Figure 14. Equipartion test for an event recorded at the station STD on the 30/12/2005: (a) observed seismogram on the E component (b) observed seismogram on the vertical component (c) envelope of the event from the E component (d) plot of the energy ratio H^2/V^2.

for coda attenuation imaging may thus be the change in the stable composition of bulk waves at higher frequencies (6 Hz and above).

The results we present are valid for volcano-tectonic earthquakes only. Once a low-period source function (3 Hz) has been convolved to the kernels, we will know if, and at which depths, we can still recover the low-period source characteristics reconstructed at shallow depths in the volcano (e.g. Matoza *et al.* 2015). Deeper resonant sources might be invisible in parts of the medium and for given frequency bands due to the scattering characteristics of the overlying unconsolidated materials (Moran *et al.* 2008). Even at shallower depths, the relative weight of path effects induced by upper volcanic structures, especially the volumes under the unconsolidated debris avalanche, could be higher than what we consider in literature. Our results support the view that unconsolidated volcanic media may be as important as fluid and magma dynamics in producing seismic coda signals inside the volcano (Bean *et al.* 2014).

6 CONCLUSIONS

The results of the Multiple Lapse Time Window Analysis (MLTWA) show that scattering attenuation prevails over absorption at low frequencies (3–6 Hz) and absorption dominates at higher frequencies (12–18 Hz). While the variations of the scattering parameters are similar to those observed in other volcanic cones, absorption is one order of magnitude lower than at active, open-conduit volcanoes. This tectonic-like feature is characteristic of low-activity or dormant volcanoes, like Mt Fuji. MSH showed no sign of activity during the 2000–2003 period: the eruption onsets 1 yr after this period (October 2004). The seismic albedo at 3 Hz is the highest ever recorded at a volcano, likely due to the unexpected influence of near-receiver scattering generating surface waves in the near and far fields.

We obtained both approximate 2-D diffusive sensitivity kernels (AD) and MLTWA-derived bulk sensitivity kernels (ETE, computed from the 3-D numerical solution of Paasschens (1997) approximation). With these kernels, we can test the spatial sensitivity of coda waves at late lapse-times and produce 2-D tomographic maps. The results of the MLTWA suggest that AD imaging can only model coda envelopes at frequencies higher than 3 HZ and late lapse times. The MLTWA parameters provide inputs to build the ETE kernels, which were down-scaled to 2-D in order to overdetermine the tomographic inversion. Both kernels depict a shift of the highest-attenuation structures from north and south of the volcano to its eastern side with increasing frequency, in correspondence with low-velocity anomalies associated to the upper magmatic systems. At low frequency (3 Hz and below) we infer that shallow unconsolidated volcanic layers as those comprised under the debris avalanche and crater are the cause of: (1) the anomalous seismic albedo (0.95); (2) the difficulty in modelling bulk-wave envelopes recorded inside the volcanic cone with a half-space model, without including surface waves and (3) the biases in diffusive and multiple-scattering kernel-dependent imaging.

Source modelling studies acknowledge the need for dedicated near-source arrays for stable measurements and reliable inferences of eruption dynamics, in particular, to avoid the influence of path attenuation on seismic measurements. This study provides a new understanding of the spatial and frequency sensitivity of late seismic signal to lateral heterogeneity. The results improve interpretations of the structures retrieved by coda attenuation imaging, once framed in the extensive geological and geophysical knowledge about the volcano. The enhanced sensitivity to near-station unconsolidated volcanic materials compared to source characteristics is evident even at very shallow depths at the lowest frequencies. Still, the results are only valid for volcano-tectonic sources; resonant source functions need to be embedded in the modelling to clarify if these sensitivities are significant when modelling low-period signals, removing biases from such crucial measurements of volcanic unrest.

ACKNOWLEDGEMENTS

Simona Gabrielli received funding from both the Scottish Alliance for Geosciences Environment and Society and the Kleinman Grant for Volcano Research to travel to the United States and perform fieldwork necessary for the interpretation of the retrieved anomalies. We thank Angel de la Torre for providing the initial code for the computation of the ETE kernels and Panayiota Sketsiou for an early revision of the paper. The revision of Carlos Vargas and an anonymous reviewer pushed us to perform a better forward modelling of the recorded intensity and improve our interpretations.

REFERENCES

Badi, G., Del Pezzo, E., Ibanez, J.M., Bianco, F., Sabbione, N. & Araujo, M., 2009. Depth dependent seismic scattering attenuation in the Nuevo Cuyo region (southern central Andes), *Geophys. Res. Lett.,* **36**(24), 1–5.

Bean, C.J., De Barros, L., Lokmer, I., Métaxian, J.-P., O?Brien, G. & Murphy, S., 2014. Long-period seismicity in the shallow volcanic edifice formed from slow-rupture earthquakes, *Nature Geoscience,* **7**(1), 71.

Bianco, F., Castellano, M., Del Pezzo, E. & Ibanez, J.M., 1999. Attenuation of short-period seismic waves at Mt Vesuvius, Italy, *J. geophys. Int.,* **138**(1), 67–76.

Brocher, T.M., Wells, R.E., Lamb, A.P. & Weaver, C.S., 2017. Evidence for distributed clockwise rotation of the crust in the northwestern united states from fault geometries and focal mechanisms, *Tectonics,* **36**(5), 787–818.

Canas, J.A., Ugalde, A., Pujades, L.G., Carracedo, J.C., Soler, V. & Blanco, M.J., 1998. Intrinsic and scattering seismic wave attenuation in the Canary Islands, *J. geophys. Res.,* **103**(B7), 15 037–15 050.

Chung, T.W., Lees, J.M., Yoshimoto, K., Fujita, E. & Ukawa, M., 2009. Intrinsic and scattering attenuation of the Mt Fuji Region, Japan, *J. geophys. Int.,* **177**(3), 1366–1382.

Cormier, V.F. & Sanborn, C.J., 2019. Trade-offs in parameters describing crustal heterogeneity and intrinsic attenuation from radiative transport modeling of high-frequency regional seismograms, *Bull. seism. Soc. Am.,* **109**(1), 312–321.

De Siena, L., Del Pezzo, E., Thomas, C., Curtis, A. & Margerin, L., 2013. Seismic energy envelopes in volcanic media: in need of boundary conditions, *J. geophys. Int.,* **195**(2), 1102–1119.

De Siena, L., Thomas, C., Waite, G.P., Moran, S.C. & Klemme, S., 2014. Attenuation and scattering tomography of the deep plumbing system of Mount St. Helens, *J. geophys. Res.,* **119**(11), 8223–8238.

De Siena, L., Calvet, M., Watson, K.J., Jonkers, A. R.T. & Thomas, C., 2016. Seismic scattering and absorption mapping of debris flows, feeding paths, and tectonic units at Mount St. Helens volcano, *Earth planet. Sci. Lett.,* **442,** 21–31.

De Siena, L., Amoruso, A., Pezzo, E.D., Wakeford, Z., Castellano, M. & Crescentini, L., 2017. Space-weighted seismic attenuation mapping of the aseismic source of Campi Flegrei 1983-1984 unrest, *Geophys. Res. Lett.,* **44**(4), 1740–1748.

Del Pezzo, E. & Bianco, F., 2010. MathLTWA: multiple lapse time window analysis using Wolfram Mathematica 7, *Comput. Geosci.,* **36**(10), 1388–1392.

Del Pezzo, E., Bianco, F., Marzorati, S., Augliera, P., D'Alema, E. & Massa, M., 2011. Depth-dependent intrinsic and scattering seismic attenuation in north central Italy, *J. geophys. Int.,* **186**(1), 373–381.

Del Pezzo, E., Bianco, F., Giampiccolo, E., Tusa, G. & Tuvé, T., 2015. A reappraisal of seismic Q evaluated at Mt. Etna volcano. Receipt for the application to risk analysis, *J. Seismol.,* **19**(1), 105–119.

Del Pezzo, E., Ibañez, J., Prudencio, J., Bianco, F. & De Siena, L., 2016. Absorption and scattering 2-D volcano images from numerically calculated space-weighting functions, *J. geophys. Int.,* **206**(2), 742–756.

Del Pezzo, E., De La Torre, A., Bianco, F., Ibanez, J., Gabrielli, S. & De Siena, L., 2018. Numerically calculated 3D space-weighting functions to image crustal volcanic structures using diffuse coda waves, *Geosciences,* **8**(5), doi:10.3390/geosciences8050175.

Del Pezzo, E., Giampiccolo, E., Tuvé, T., Di Grazia, G., Gresta, S. & Ibáñez, J.M., 2019. Study of the regional pattern of intrinsic and scattering seismic attenuation in Eastern Sicily (Italy) from local earthquakes, *J. geophys. Int.,* **218**(2), 1456–1468.

Dutta, U., Biswas, N.N., Adams, D.A. & Papageorgiou, A., 2004. Analysis of S-wave attenuation in south-central Alaska, *Bull. seism. Soc. Am.,* **94**(1), 16–28.

Eide, C.H., Schofield, N., Lecomte, I., Buckley, S.J. & Howell, J.A., 2018. Seismic interpretation of sill complexes in sedimentary basins: implications for the sub-sill imaging problem, *J. geol. Soc.,* **175**(2), 193–209.

Fehler, M., Roberts, P. & Fairbanks, T., 1988. A temporal change in coda wave attenuation observed during an eruption of Mount St. Helens, *J. geophys. Res.,* **93**(7), 4367–4373.

Fehler, M., Hoshiba, M., Sato, H. & Obara, K., 1992. Separation of scattering and intrinsic attenuation for the Kanto-Tokai region, Japan, using measurements of S-wave energy versus hypocentral distance, *J. geophys. Int.,* **108**(3), 787–800.

Galluzzo, D., La Rocca, M., Margerin, L., Del Pezzo, E. & Scarpa, R., 2015. Attenuation and velocity structure from diffuse coda waves: constraints from underground array data, *Phys. Earth planet. Inter.,* **240,** 34–42.

Hansen, S.M., Schmandt, B., Levander, A., Kiser, E., Vidale, J.E., Abers, G.A. & Creager, K.C., 2016. Seismic evidence for a cold serpentinized mantle wedge beneath Mount St Helens, *Nat. Commun.,* **7,** 13242.

Hennino, R., Trégourès, N., Shapiro, N.M., Margerin, L., Campillo, M., van Tiggelen, B.A. & Weaver, R.L., 2001. Observation of equipartition of seismic waves, *Phys. Rev. Lett.,* **86,** 3447–3450.

Hill, G.J., Caldwell, T.G., Heise, W., Chertkoff, D.G., Bibby, H.M., Burgess, M.K., Cull, J.P. & Cas, R.A.F., 2009a. Distribution of melt beneath Mount St Helens and Mount Adams inferred from magnetotelluric data, *Nat. Geosci.,* **2**(11), 785–789.

Hill, J., Tetzlaff, D., Curtis, A. & Wood, R., 2009b. Modeling shallow marine carbonate depositional systems, *Comput. Geosci.,* **35**(9), 1862–1874.

Iverson, R.M. *et al.*, 2006. Dynamics of seismogenic volcanic extrusion at Mount St Helens in 2004-05, *Nature,* **444**(7118), 439–443.

King, T., Benson, P., De Siena, L. & Vinciguerra, S., 2017. Investigating the apparent seismic diffusivity of near-receiver geology at Mount St. Helens Volcano, USA, *Geosciences,* **7**(4), 130.

Kiser, E. *et al.*, 2016. Magma reservoirs from the upper crust to the Moho inferred from high-resolution Vp and Vs models beneath Mount St. Helens, Washington State, USA, *Geology,* **44**(6), 411–414.

Kiser, E., Levander, A., Zelt, C., Schmandt, B. & Hansen, S., 2018. Focusing of melt near the top of the Mount St. Helens (USA) magma reservoir and its relationship to major volcanic eruptions, *Geology,* **46**(9), 775.

Larose, E., Derode, A., Clorennec, D., Margerin, L. & Campillo, M., 2005a. Passive retrieval of Rayleigh waves in disordered elastic media, *Phys. Rev. E,* **72**(4), 046607.

Larose, E., Khan, A., Nakamura, Y. & Campillo, M., 2005b. Lunar subsurface investigated from correlation of seismic noise, *Geophys. Res. Lett.,* **32**(16), 1–4.

Lees, J.M., 1992. The magma system of Mount St. Helens: non-linear high resolution P-wave tomography, *J. Volc. Geotherm. Res.,* **53**(1-4), 103–116.

Lees, J.M., 2007. Seismic tomography of magmatic systems, *J. Volc. Geotherm. Res.,* **167**(1–4), 37–56.

Lehto, H.L., Roman, D.C. & Moran, S.C., 2013. Source mechanisms of persistent shallow earthquakes during eruptive and non-eruptive periods between 1981 and 2011 at Mount St. Helens, Washington, *J. Volc. Geotherm. Res.,* **256,** 1–15.

Lemzikov, M.V., 2008. Estimation of shear-wave attenuation characteristics for the Klyuchevskoi volcanic edifice, *J. Volcanol. Seismol.,* **2**(2), 108–117.

Londono, J.M., 1996. Temporal change in coda Q at Nevado del Ruiz Volcano, Colombia, *J. Volc. Geotherm. Res.,* **73**(1–2), 129–139.

Margerin, L., Planès, T., Mayor, J. & Calvet, M., 2015. Sensitivity kernels for coda-wave interferometry and scattering tomography: theory and numerical evaluation in two-dimensional anisotropically scattering media, *J. geophys. Int.,* **204**(1), 650–666.

Matoza, R.S. & Chouet, B.A., 2010. Subevents of long-period seismicity: Implications for hydrothermal dynamics during the 2004-2008 eruption of Mount St. Helens, *J. geophys. Res.,* **115**(12), 1–26.

Matoza, R.S. *et al.*, 2015. Source mechanism of small long-period events at Mount St. Helens in July 2005 using template matching, phase-weighted stacking, and full-waveform inversion, *J. geophys. Res.,* **120**(9), 6351–6364.

Mayeda, K., Koyanagi, S., Hoshiba, M., Aki, K. & Zeng, Y., 1992. A comparative study of scattering, intrinsic, and coda q- 1 for Hawaii, Long Valley, and central California between 1.5 and 15.0 Hz, *J. geophys. Res.,* **97**(B5), 6643–6659.

Moran, S.C., Malone, S.D., Qamar, A.I., Thelen, W.A., Wright, A.K. & Caplan-Auerbach, J., 2008. Seismicity associated with renewed dome building at Mount St. Helens, 2004–2005, in *A Volcano Rekindled: The Renewed Eruption of Mount St. Helens, 2004–2006,* Vol. 1750, pp. 27–60, US Geological Survey Menlo Park.

Musumeci, C., Gresta, S. & Malone, S.D., 2002. Magma system recharge of Mount St. Helens from precise relative hypocenter location of microearthquakes, *J. geophys. Res.,* **107**(B10), ESE 16–1-ESE 16-9.

Obermann, A., Planès, T., Larose, E. & Campillo, M., 2013. Imaging preeruptive and coeruptive structural and mechanical changes of a volcano with ambient seismic noise, *J. geophys. Res.,* **118**(12), 6285–6294.

Paasschens, J., 1997. Solution of the time-dependent Boltzmann equation, *Phys. Rev. E,* **56**(1), 1135–1141.

Pacheco, C. & Snieder, R., 2005. Time-lapse travel time change of multiply scattered acoustic waves, *J. acoust. Soc. Am.,* **118**(3), 1300–1310.

Padhy, S. & Subhadra, N., 2013. Separation of intrinsic and scattering seismic wave attenuation in northeast india, *J. geophys. Int.,* **195**(3), 1892–1903.

Pallister, J.S., Hoblitt, R.P., Crandell, D.R. & Mullineaux, D.R., 1992. Mount St. Helens a decade after the 1980 eruptions: magmatic models, chemical cycles, and a revised hazards assessment, *Bull. Volcanol.,* **54**(2), 126–146.

Parsons, T. *et al.*, 2006. Crustal structure of the Cascadia Fore Arc of Washington, USGS Professional Paper.

Pisconti, A., Pezzo, E.D., Bianco, F. & Lorenzo, S.D., 2015. Seismic Q estimates in Umbria Marche (Central Italy): hints for the retrieval of a new attenuation law for seismic risk, *J. geophys. Int.,* **201** (3), 1370–1382.

Prudencio, J., Del Pezzo, E., García-Yeguas, A. & Ibáñez, J.M., 2013a. Spatial distribution of intrinsic and scattering seismic attenuation in active volcanic islands – I: model and the case of tenerife Island, *J. geophys. Int.,* **195**(3), 1942–1956.

Prudencio, J., Ibáñez, J.M., García-Yeguas, A., Del Pezzo, E. & Posadas, A.M., 2013b. Spatial distribution of intrinsic and scattering seismic attenuation in active volcanic islands – II: deception island images, *J. geophys. Int.,* **195**(3), 1957–1969.

Prudencio, J., Ibáñez, J.M., Del Pezzo, E., Martí, J., García-Yeguas, A. & De Siena, L., 2015. 3D Attenuation tomography of the volcanic Island of Tenerife (Canary Islands), *Surv. Geophys.,* **36**(5), 693–716.

Prudencio, J., Aoki, Y., Takeo, M., Ibáñez, J.M., Del Pezzo, E. & Song, W.Z., 2017. Separation of scattering and intrinsic attenuation at Asama volcano (Japan): evidence of high volcanic structural contrasts, *J. Volc. Geotherm. Res.,* **333-334,** 96–103.

Prudencio, J., Manga, M. & Taira, T., 2018. Subsurface structure of Long Valley Caldera imaged with seismic scattering and intrinsic attenuation, *J. geophys. Res.,* **123**(7), 5987–5999.

Przybilla, J., Wegler, U. & Korn, M., 2009. Estimation of crustal scattering parameters with elastic radiative transfer theory, *J. geophys. Int.,* **178**(2), 1105–1111.

Sanborn, C.J., Cormier, V.F. & Fitzpatrick, M., 2017. Combined effects of deterministic and statistical structure on high-frequency regional seismograms, *J. geophys. Int.,* **210**(2), 1143–1159.

Sato, H., Fehler, M.C. & Maeda, T., 2012. *Seismic Wave Propagation and Scattering in the Heterogeneous Earth,* Vol. **496,** Springer.

Scandone, R. & Malone, S.D., 1985. Magma supply, magma discharge and readjustment of the feeding system of mount St. Helens during 1980, *J. Volc. Geotherm. Res.,* **23**(3-4), 239–262.

Schilling, S.P., Carrara, P.E., Thompson, R.A. & Iwatsubo, E.Y., 2004. Posteruption glacier development within the crater of Mount St. Helens, Washington, USA, *Quater. Res.,* **61**(3), 325–329.

Stanley, W.D., Johnson, S.Y., Qamar, A.I., Weaver, C.S. & Williams, J.M., 1996. Tectonics and seismicity of the Southern Washington cascade range, *Bull. seism. Soc. Am.,* **86**(1A), 1.

Tramelli, A., del Pezzo, E. & Fehler, M.C., 2009. 3D scattering image of Mt. Vesuvius, *Bull. seism. Soc. Am.,* **99**(3), 1962–1972.

Tusa, G., Malone, S.D., Giampiccolo, E., Gresta, S. & Musumeci, C., 2004. Attenuation of short-period P waves at Mount St. Helens, *Bull. seism. Soc. Am.,* **94**(4), 1441–1455.

Ugalde, A., Carcolé, E. & Vargas, C.A., 2010. S-wave attenuation characteristics in the Galeras volcanic complex (south western Colombia), *Phys. Earth planet. Inter.,* **181**(3–4), 73–81.

Vallance, J., Schneider, D. & Schilling, S., 2008. Growth of the 2004-2006 Lava-Dome Complex at Mount St. Helens, Washington, A Volcano Rekindled: The Renewed Eruption of Mount St. Helens 2004-2006, U.S. Geological Survey Professional Paper 1750, pp. 169–208.

Waite, G.P. & Moran, S.C., 2009. VP structure of Mount St. Helens, Washington, USA, imaged with local earthquake tomography, *J. Volc. Geotherm. Res.,* **182**(1–2), 113–122.

Weaver, C. & Smith, S., 1983. Regional tectonic and earthquake hazard implications of a crustal fault zone in southwestern Washington, *J. geophys. Res.,* **35**(9), 2857–2869.

Wegler, U., 2003. Analysis of multiple scattering at Vesuvius volcano, Italy, using data of the TomoVes active seismic experiment, *J. Volc. Geotherm. Res.,* **128**(1–3), 45–63.

Wegler, U. & Lühr, B.G., 2001. Scattering behaviour at Merapi volcano (Java) revealed from an active seismic experiment, *J. geophys. Int.,* **145**(3), 579–592.

SUPPORTING INFORMATION

Supplementary data are available at *GJI* online.

Figure S1. Plot of the normalized energy integral versus the hypocentral distance range of 0–20 km: blue, orange and green dots represent first, second and third window, respectively (Fig. 3), while the continuous lines are the best fit calculated with the solution of the transport equation in the uniform half-space assumption. At 3 Hz, the theoretical energy is missing because there are not enough data to define a trend and so a fitting line.

Figure S2. Plot of the normalized energy integral versus the hypocentral distance range of 0–50 km: blue, orange and green dots represent, first, second and third window, respectively (Fig. 3), while the continuous lines are the best fit calculated with the solution of the transport equation in the uniform half-space assumption

Figure S3. L-curves used to invert for Q_c^1 c at 3 and 18 Hz for the AD kernels. The stability of the solution is tested changing the corner parameter (red dot: 0.09) to those about one order of magnitude above and below it (black dots).

Figure S4. (a) Resolution for the AD kernel with damping parameter of 0.009; (b) Coda attenuation mapping for 3, 6 and 18 Hz. A grey mask covers the unresolved anomalies. The seismicity and the stations are plotted on the output and on the 3 Hz imaging.

Figure S5. (a) Resolution for the AD kernel with damping parameter of 0.26; (b) Coda attenuation for 3, 6 and 18 Hz. A grey mask covers the unresolved anomalies. The seismicity and the stations are plotted on the output and on the 3 Hz imaging.

Figure S6. L-curves used to invert for Q_c^1 c at 3 Hz with the ETE kernels. The stability of the solution is tested changing the corner parameter between 0.7, 0.07 (red dot) and 0.007. 0.07 is the autopicked corner parameter.